

Optical Fiber-based γ -Photon Biosensor for Real-Time Pre-clinical Evaluation of Cancer-Targeting Radiopharmaceuticals

Rahul Lall



Electrical Engineering and Computer Sciences
University of California, Berkeley

Technical Report No. UCB/EECS-2024-41

<http://www2.eecs.berkeley.edu/Pubs/TechRpts/2024/EECS-2024-41.html>

May 1, 2024

Copyright © 2024, by the author(s).
All rights reserved.

Permission to make digital or hard copies of all or part of this work for personal or classroom use is granted without fee provided that copies are not made or distributed for profit or commercial advantage and that copies bear this notice and the full citation on the first page. To copy otherwise, to republish, to post on servers or to redistribute to lists, requires prior specific permission.

Acknowledgement

I would like to acknowledge my advisors Dr. Mekhail Anwar and Dr. Ali Niknejad for their continual support and mentorship in pursuing my Master's and PhD in EECS. I would also like to thank my parents, Pradeep and Rekha Lall, and my sister, Malvika Lall, for their continual support, encouragement, and advice.

**Optical Fiber-based γ -Photon Biosensor for Real-Time Pre-clinical
Evaluation of Cancer-Targeting Radiopharmaceuticals**

by Rahul Kartikeya Lall

Research Project

Submitted to the Department of Electrical Engineering and Computer Sciences of the University of California, Berkeley, in partial satisfaction of the requirements for the degree of **Master of Science, Plan II**.

Approval for the Report and Comprehensive Examination:

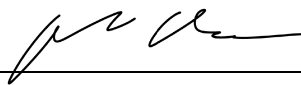
Committee:



Professor Ali Niknejad
Research Advisor

12/15/23

(Date)



Professor Mekhail Anwar
Research Advisor

12/15/23

(Date)

Optical Fiber-based γ -Photon Biosensor for Real-Time Pre-clinical Evaluation of
Cancer-Targeting Radiopharmaceuticals

by

Rahul Kartikeya Lall

A dissertation submitted in partial satisfaction of the
requirements for the degree of

Master of Science

in

Electrical Engineering and Computer Science (EECS)

in the

Graduate Division

of the

University of California, Berkeley

Committee in charge:
Professor Ali Niknejad
Professor Mekhail Anwar

Fall 2023

Optical Fiber-based γ -Photon Biosensor for Real-Time Pre-clinical Evaluation of
Cancer-Targeting Radiopharmaceuticals

Copyright 2023
by
Rahul Kartikeya Lall

Abstract

Optical Fiber-based γ -Photon Biosensor for Real-Time Pre-clinical Evaluation of
Cancer-Targeting Radiopharmaceuticals

by

Rahul Kartikeya Lall

Master of Science in Electrical Engineering and Computer Science (EECS)

University of California, Berkeley

Professor Ali Niknejad
Professor Mekhail Anwar

Cancer radiopharmaceutical therapies (RPTs) have demonstrated great promise in the treatment of neuroendocrine and prostate cancer, giving hope to late-stage metastatic cancer patients with currently very few treatment options. These therapies have sparked a large amount of interest in pre-clinical research due to their ability to target metastatic disease, with many research efforts focused towards developing and evaluating targeted RPTs for different cancer types in *in vivo* models. Here we describe a method for monitoring real-time *in vivo* binding kinetics for the pre-clinical evaluation of cancer RPTs. Recognizing the significant heterogeneity in biodistribution of RPTs among even genetically identical animal models, this approach offers long-term monitoring of the same *in vivo* organism without euthanasia in contrast to *ex vivo* tissue dosimetry, while providing high temporal resolution with a low-cost, easily assembled platform, that is not present in small-animal SPECT/CTs. The method utilizes the developed optical fiber-based γ -photon biosensor, characterized to have a wide linear dynamic range with Lutetium-177 (^{177}Lu , Lu-177) activity (0.5-500 $\mu\text{Ci/mL}$), a common radioisotope used in cancer RPT. The probe's ability to track *in vivo* uptake relative to SPECT/CT and *ex vivo* dosimetry techniques was verified by administering Lu-177-PSMA-617 to mouse models bearing human prostate cancer tumors (PC3-pip, PC3-flu). With this method for monitoring RPT uptake, it is possible to evaluate changes in tissue uptake at temporal resolutions less than 1 minute to determine RPT biodistribution in pre-clinical models and better understand dose relationships with tumor ablation, toxicity, and recurrence when attempting to move therapies towards clinical trial validation.

Contents

Contents	i
List of Figures	iii
List of Tables	vii
1 Introduction	1
1.1 Cancer, Staging, and Therapies	1
1.2 Radiopharmaceutical Therapy (RPT)	2
1.3 Promise of RPT in Treatment of Metastatic Prostate Cancer and Beyond	4
1.4 Need for Better Pre-Clinical <i>In Vivo</i> Dosimetry in RPT	7
1.5 State-of-Art in Pre-Clinical <i>In Vivo</i> Dosimetry	8
2 Design of Optical Fiber-Based γ Photon Biosensor	12
2.1 Design Overview	12
2.2 γ -Photon Scintillator	13
2.3 Visible Light Shielding	15
2.4 Characterization of γ -Photon Biosensor	15
2.5 Distance Transfer Function Derivation	19
2.6 Lead Shielding	19
3 Applying the Optical Fiber-Based Biosensor <i>In Vivo</i>	20
3.1 <i>In Vivo</i> Mice Experimental Procedures	20
3.2 Radiolabelling of ^{177}Lu -PSMA-617	21
3.3 SPECT/CT Acquisitions	23
3.4 <i>Ex Vivo</i> Biodistribution	23
4 Tracking Real-Time Tumor Binding Kinetics in <i>In Vivo</i> Models	24
4.1 Visualizing Real-Time Tumor Binding Kinetics	24
4.2 Quantifying Radiopharmaceutical Uptake and Excretion Rates	26
4.3 Calculating Therapeutic Ratio	26
4.4 Comparison of Measured Tumor Binding Kinetics to State-of-Art Pre-clinical Dosimetry	26

5	Tracking Tumor and Kidney Binding Kinetics Continuously in the Same <i>In Vivo</i> Model	29
5.1	Real-Time Tumor and Kindey Binding Kinetics	29
5.2	Approximating Minimum Acquisition Time	29
6	Utility of Proposed Biosensor Platform for Pre-clinical Evaluation of Radiopharmaceutical Therapy	32
6.1	Utility in RPT	32
6.2	System Cost and Scalability	32
6.3	Limitations	33
6.4	Comparison to RPT Biosensors in Literature	34
7	Conclusions & Future Work	36
7.1	Scope of Presented Work	36
7.2	Future Work	36
8	Bibliography	39

List of Figures

1.1	Methods of Cancer Therapy. Local cancer therapies are focused on early stage cancer treatment. Systemic cancer therapies are focused on late stage cancer treatment.	2
1.2	Radiopharmaceutical Therapy Concept. Given a PSMA+ prostate cancer tumor that has begun to metastasize, one targeted treatment option is to conjugate a PSMA targeting molecule to a radioisotope (Lu-177 and Ac-225 commonly) to specifically radiate these cancer cells. The high LET radiation causes double strand breaks (DSBs), and the γ photons are imageable to understand RPT biokinetics.	3
1.3	Current Metastatic Castration Resistant Prostate Cancer Treatment Pipeline. Even with this comprehensive treatment pipeline, it is apparent that many prostate cancer patients progress, and new targeted treatments are necessary to help improve the quality and treatment response of each patient.	5
1.4	Promise of RPT as Seen in Literature. Figures from Kratochwil et al. 2016 that describe two patients that underwent either Lu-177 β -RPT or Ac-225 α -RPT. Both panels are scintigraphy images before and after RPT, with the dark spots present pre-therapy indicating tumors or pockets of metastatic disease. It is apparent that all of these metastatic sites disappear from the scintigraphy scan post-therapy.	6
1.5	Optimizing Cancer Radiotherapy in a Patient-Specific Manner. Due to the heterogeneity in the clinical presentation of cancer and the fact that many patients become resistant to certain types of therapy (anti-androgen hormone therapy, chemotherapy, etc.), cancer therapy is moving away from traditional single dosing to adaptive personalized dosing for every patient. This helps prevent proliferation of resistant cells, improve treatment delivery to target cells, and reduce toxicity.	9

1.6	Conceptual Workflow and Optical Fiber γ -Photon Biosensor Design. (a) An <i>in vivo</i> model with two tumors from different cancer cell lines is administered a RPT and (b) measured using the proposed γ biosensor platform at very fine intervals with short acquisition times. (c) At the last time point, a single SPECT/CT or <i>ex vivo</i> γ counting is done to convert the γ counts from the biosensor to %IA/mL. (d) Optical sensing front end with compacted Y_2O_3 -Eu doped phosphor at face of optical fiber that is surrounded with lead tape and optical tape. (e) Optical fiber is interfaced to readout circuitry, including APDs, amplifiers, level-shifters, digital counters, and data readout.	10
2.1	Optimizing Scintillating Phosphor Thickness for Desired Sensitivity and Dynamic Range (a) IVIS image generated (with an 180 s integration time) of ^{133}Ba point source planted on disk with 3D printed fiber cap containing optimized 500 μm thick $Y_2O_3 - Eu$ doped phosphor. This was repeated for 8 different thicknesses. (b) Normalized total counts from IVIS versus scintillator thickness over a 180 s integration time.	13
2.2	Measuring Scintillator Afterglow. Dark count of each APD before a full serial dilution experiment with 10 minute exposure per vial vs. dark count after the full serial dilution experiment for (a) probe 1 and (b) probe 2 used for the <i>in vivo</i> experiments.	14
2.3	Visible Light Shielding of Optical-Fiber Biosensor Dark count of each APD in a light-sealed box vs. in a well lit room for (a) probe 1 and (b) probe 2 used for the <i>in vivo</i> experiments.	15
2.4	Characterization of Optical Fiber Biosensor with Lu-177 Activity (a) Lu-177 serial dilution experimental setup. (b) Lu-177 serial dilution real-time transient results of γ CPS with activities ranging from 0.5 to 500 $\mu Ci/mL$. (c) Poisson fit of recorded γ CPS distribution, as count variation can be attributed to the Poisson nature of radioactive decay. (d) Average CPS from the proposed system is highly linear with activity, for activities ranging from 0.5 μCi to 500 μCi . (e) The absolute error in CPS for the activity range of interest (f) Sensitivity calibration of the two biosensors that were used for the majority of this study, using the setup in (c) as well	16
2.5	Characterization of Optical Fiber Biosensor with Ac-225 Activity Measured CPS from outside of a Ac-225 2x dilution with the proposed system. Each vial was measured for 30 minutes. (a) Average CPS from the proposed system is highly linear with ^{225}Ac activity, for activities ranging from 7.8 nCi to 500 nCi in 1 mL. (b) The absolute error in CPS for the activity range of interest.	17

- 2.6 Design of Lead Shielding to Mitigate Organ-to-Organ Cross-Talk (a) Experimental setup to test the developed system’s transfer function with distance and to test if the lead thickness was sufficient to prevent cross-talk of recorded gamma CPS. A 365 μCi Lu-177 vial was swept from 0 to 3 cm away from the sensor face as well as 0 to 6 cm laterally. (b) Transfer function between recorded γ CPS and distance away from the sensor face. (c) Probability of detection for the weighted average energy γ photon from Lu-177 for various thicknesses of lead. (d) Measurement of lateral distance transfer function with and without 1 mm thick lead tape. 18
- 3.1 *In Vivo* Experimental Setup.(a) SQ injection of PC3-pip and PC3-flu cells into flanks of mice M1-M16. (b) After 14 days, the two tumors grew to be palpable and 600 μCi of Lu-177-PSMA-617 was administered to mice M1-M16 via tail-vein injection. (c) One γ biosensor is placed behind each tumor in mice M1-M16, while under anesthesia for 2 hours. M1-M15 are monitored at a single time point post injection, but M16 is chronically monitored over five timepoints post-injection. M16 also has two additional probes placed vertically above the left and right kidneys to track kidney (OAR) uptake and clearance. (d) Immediately after their respective 2-hour measurement, mouse M1-M15 are euthanized and a SPECT/CT is taken. M16 is not euthanized and is chronically monitored, with a SPECT/CT taken after each γ biosensor acquisition. (e) The tumors of mice M1-M15 are dissected, and a small sample of the tumor is used to perform *ex vivo* dosimetry. 21
- 3.2 Implemented *In Vivo* Experimental Setup. (a) Athymic nude mouse (M1-M15) with bilateral tumors (PC3-pip, PC3-flu). Each tumor was monitored with the proposed γ biosensor for 2 hours at a specific time point post-injection. M16 has the same experimental setup but with 2 additional γ biosensors on each kidney. (b) Small-animal SPECT/CT machine used to perform state-of-art imaging based dosimetry. (c) HIDEX biodistribution machine used for state-of-art *ex vivo* dosimetry. (d) The tumors of mice M1-M15 are dissected after the SPECT/CT scan, and a small sample of each tumor is placed in individual vials to perform *ex vivo* dosimetry. 22
- 4.1 Representative SPECT Scans and γ Probe Counts of PC3-pip and PC3-flu Tumors of M1-M15.(a) SPECT scans show progression of ^{177}Lu -PSMA-617 activity accumulation in PC3-pip and PC3-flu tumors at five time points taken at the end of every custom γ probe recording. (b) Real-time γ probe recordings over the two hour recording period before the respective SPECT scan was taken. (c) Average slope of transient waveforms per hour from 6-50 hours post injection. (d) Derived chronic biodistribution curve from proposed system over 50 hours post injection. (e) Therapeutic ratio between the PC3-pip tumor counts to the PC3-flu tumor counts over 50 hours post injection. 25

4.2	Evaluation of Biosensor Accuracy with SPECT/CT and <i>ex vivo</i> Dosimetry for M1-M15. Biodistribution curve from (a) SPECT/CT and (b) <i>ex vivo</i> dosimetry. (c) Comparison of CPS with the tumor activity normalized to the tumor volume from SPECT. (d) %IA/mL error histogram between the biosensor platform and SPECT/CT. (e) Comparison of CPS with the tumor activity normalized to the tumor volume from <i>ex vivo</i> dosimetry. (f) %IA/mL error histogram between the biosensor platform and <i>ex vivo</i> dosimetry.	27
5.1	Monitoring of a Single Mouse (M16) Over Multiple Time Points. Biodistribution curve from (a) the proposed biosensor platform and (b) SPECT/CT for both tumors and kidneys. (c) Comparison of CPS from the biosensor platform with the activity from SPECT. (d) %IA/mL error histogram between the biosensor platform and SPECT/CT. Convergence in (e) average %IA/mL error, (f) R2, (g) and linear fit slope with acquisition time before SPECT/CT.	30
7.1	Wearable, Integrated Sparse SPECT for Continuous, Real-Time Dosimetry in RPT	37

List of Tables

6.1 Comparison Table of Related Works in Literature 35

Acknowledgments

I would like to acknowledge my advisors Dr. Mekhail Anwar and Dr. Ali Niknejad for their continual support and mentorship in pursuing my Master's and PhD in EECS. I would also like to thank my parents, Pradeep and Rekha Lall, and my sister, Malvika Lall, for their continual support, encouragement, and advice.

Chapter 1

Introduction

1.1 Cancer, Staging, and Therapies

Cancer refers to a class of diseases that is characterized by abnormal and uncontrollable cell growth and multiplication. These cells have the potential to spread by invading neighboring tissues, leading to poor prognosis and survival after intervention. The severity of disease is commonly characterized through the process of cancer staging, which involves the physician evaluating where a cancer is located, its size, how far it has grown into nearby tissues, and if it has spread to nearby lymph nodes or other parts of the body. Before beginning any type of cancer therapy, doctors will choose from a variety of diagnostic tests including but not limited to physical exams (e.g. palpitation for nodules or lumps), blood work (e.g. prostate specific antigen (PSA) levels, white blood cell (WBC) counts, etc.), imaging (computed tomography (CT), positron emission tomography (PET), ultrasound (US), etc.), and cell analysis (e.g. biopsy for histology analysis) to correctly stage the cancer and layout the best path forward for patient treatment (Figure 1.1).

Cancer that is diagnosed at an early stage (e.g. single tumor site) is usually treated with a type of local cancer therapy such as surgery or external beam radiotherapy. At this stage, the cancer cells are highly localized to a single tumor site, and this tumor can be surgically excised and/or treated with high flux gamma (γ) photon, beta (β) particle, proton (p_+), or neutron (n_0) radiation therapy from a localized external beam. As cancer stage progresses, cancer cells begin to spread or metastasize by invading neighboring tissues forming many pockets of disease. At this stage, it becomes infeasible to locally treat each lesion and systemic approaches to cancer therapy are taken instead, including chemotherapy, hormone therapy, and targeted therapy. Chemotherapy involves intravenously administering a chemical pharmaceutical that non-specifically slows the growth of fast-dividing cells, including both cancer and healthy cells. Although chemotherapy has shown promise in the treatment of later stage cancer patients, it is associated with a large amount of side effects and toxicity due to its non-specificity to cancer cells. Similarly, hormone therapy is systemically administered and focuses on slowing the growth of cells whose accelerated growth is associated with

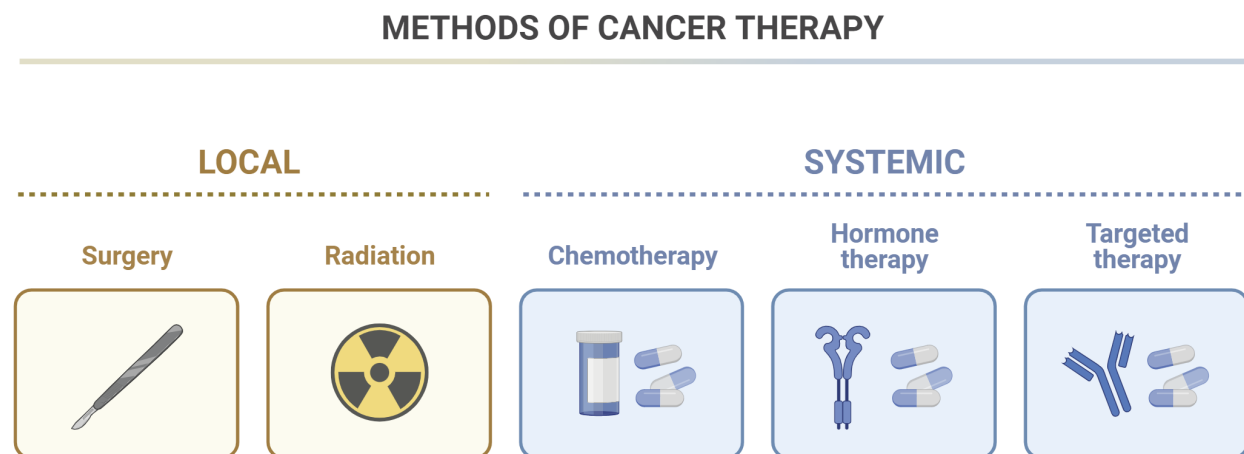


Figure 1.1: Methods of Cancer Therapy. Local cancer therapies are focused on early stage cancer treatment. Systemic cancer therapies are focused on late stage cancer treatment.

elevated levels of androgens, such as testosterone in prostate cancer. Similar to chemotherapy, hormone therapy is associated with many side effects due to its non-specificity to cancer cells and has shown poor benefits in metastatic disease. In recent years, there has been a significant amount of work towards the development of targeted therapies which couple a cancer-targeting molecule to anti-cancer drugs or radioisotopes to increase the specificity and treatment response in patients with highly metastatic disease. Here, I focus on the radiation subset of targeted therapies called radiopharmaceutical therapies (RPT), due to the plethora of promising results in clinical trials, with the FDA approving the first targeted therapy for the treatment of metastatic castration resistant prostate cancer (mCRPC) in 2021 (Sartor et al. 2021).

1.2 Radiopharmaceutical Therapy (RPT)

Overview

Radiopharmaceutical therapy, or RPT, describes systemic cancer treatment involving the targeted delivery of radiation to tumor cells. This is done by identifying and engineering a molecule (e.g., antibody, small molecule) that specifically binds to a biomarker or protein that is expressed differentially in cancer cells when compared to normal, healthy cells. For example, in metastatic prostate cancer, many patients have lesions that express PSMA at very high levels, or are PSMA+. An antibody that selectively binds to PSMA (PSMA-617) can be conjugated to a radioisotope to form a radiopharmaceutical or radioimmunoconjugate.

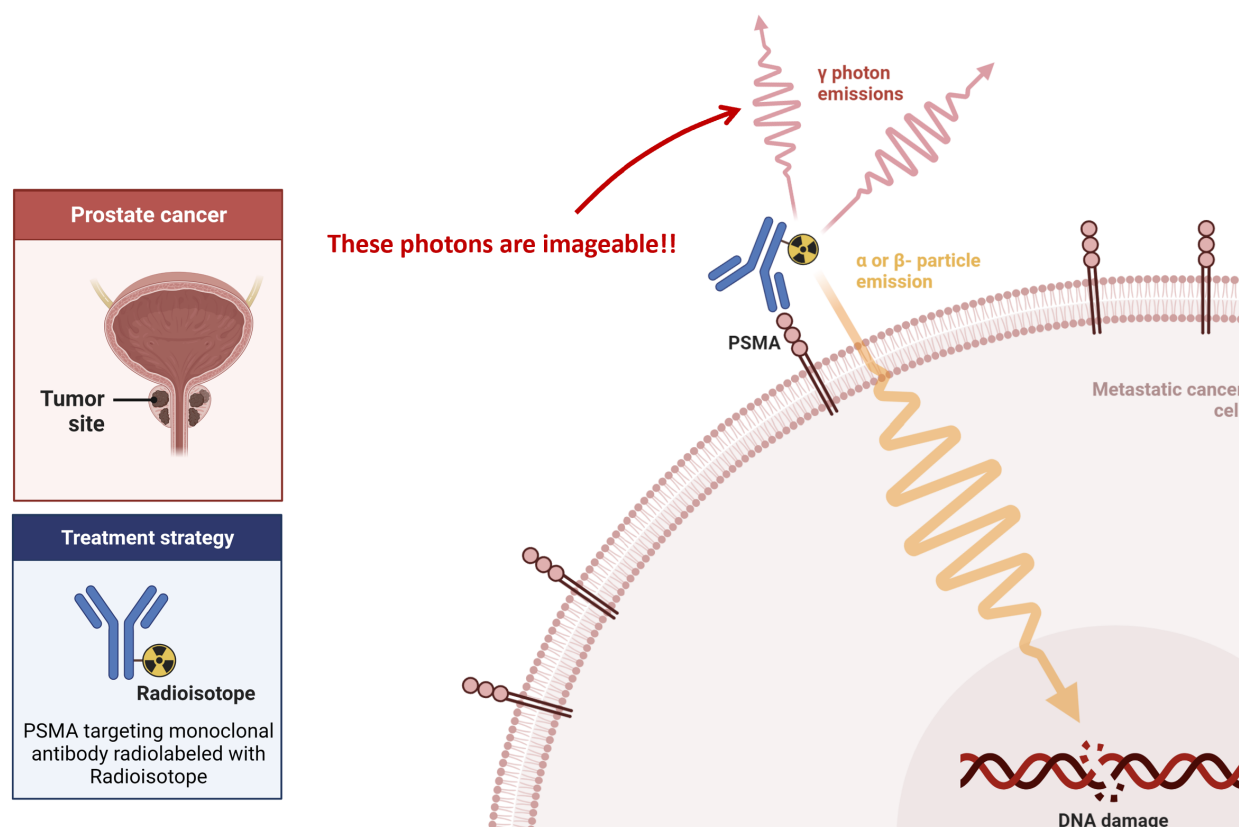


Figure 1.2: Radiopharmaceutical Therapy Concept. Given a PSMA+ prostate cancer tumor that has begun to metastasize, one targeted treatment option is to conjugate a PSMA targeting molecule to a radioisotope (Lu-177 and Ac-225 commonly) to specifically radiate these cancer cells. The high LET radiation causes double strand breaks (DSBs), and the γ photons are imageable to understand RPT biokinetics.

Radiation Physics

There are three common types of ionizing radiation that are used in conjunction with small-molecules or antibodies to engineer radiopharmaceuticals: (1) alpha (α) particles, (2) beta (β) particles, (3) gamma (γ) photons.

α particles are ionized helium atoms and have very high linear energy transfer (LET). High LET particles deposit a significant amount of their energy in a very small amount of distance (on the scale of $\text{MeV}/\mu\text{m}$). Because of this, alpha particles deposit all of their energy within, and can only traverse, a few microns in tissue. β particles are high energy electrons that are high LET particles, but have a much lower LET compared to α particles. β particles deposit their energy on the scale of $\text{keV}/\mu\text{m}$, allowing for them to traverse a few millimeters in tissue. γ photons are high energy photons there are low LET particles.

Low LET particles are sparsely ionizing, losing energy on the order of keV/cm to keV/m in tissue, meaning that they can traverse meters without losing a significant amount of energy.

Mechanism of Action

In designing a radiopharmaceutical for targeted cancer therapy, the radioisotope that makes up this conjugate has to be carefully selected based on its decay scheme (e.g. what types of radiation it emits to decay to a stable atomic state). Typically the radioisotopes used in RPT are characterized to be α and/or β emitters, with a minority of γ photon decay chains.

The radiopharmaceutical is administered to patients intravenously, where it distributes throughout the body by utilizing the blood stream. The radiopharmaceutical will begin to selectively accumulate on the tumor cells that express the biomarker or protein of interest, with the rest of the unbound treatment being rapidly excreted from the body through the kidneys or liver. When the radiopharmaceutical binds to a cancer cell, the α and/or β particles are in close enough proximity to the nucleus of that cancer cell and nearby cancer cells to deposit a significant amount of their energy into the cell's DNA. α particles will cause double-strand breaks (DSBs) in the DNA with high probability, and β particles have a higher probability of causing single stranded breaks (SSBs) in the DNA. Frequent DSBs and SSBs will trigger cell repair mechanisms and initiate cell apoptosis (e.g., programmed cell death). High LET radiation can also indirectly cause cell death by creating free radicals from energy deposition in the water molecules present in tissue. These free radicals will cause cytotoxicity, and subsequent cell death. The minority γ photons will be able to travel out of the body, and these photons can be measured and used for imaging non-invasively to quantify the biodistribution of the radiopharmaceutical (Figure 1.2).

Quality and Safety of Administration

RPT aims to maximize the radiation dose administered to all tumors and lesions of interest to maximize therapeutic benefit, while minimizing undesired dose deposition in healthy, organs at risk (OAR) that could cause toxicity during the course of treatment. OARs include all organs that are (1) transiently exposed to the radiopharmaceutical during administration (e.g., blood, bone marrow), (2) excretory organs that eliminate the radiopharmaceutical from the body (e.g., kidneys, liver), and (3) non-target organs that are unnecessarily radiated due to non-specific binding of the radiopharmaceutical.

1.3 Promise of RPT in Treatment of Metastatic Prostate Cancer and Beyond

Virtually incurable, 20% of all prostate cancer deaths are now due to metastatic castration-resistant prostate cancer (mCRPC) (Scher et al. 2015), despite significant advances in androgen inhibitors (de Bono et al. 2011, Scher 2012), and effective treatments remain an

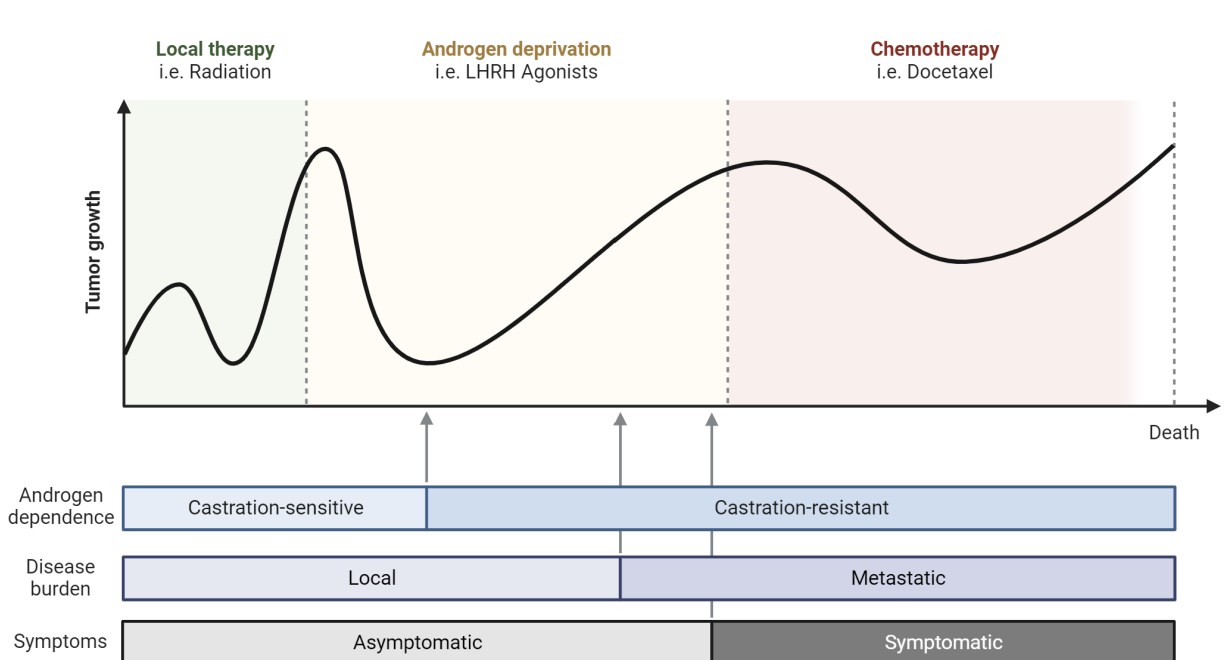


Figure 1.3: Current Metastatic Castration Resistant Prostate Cancer Treatment Pipeline. Even with this comprehensive treatment pipeline, it is apparent that many prostate cancer patients progress, and new targeted treatments are necessary to help improve the quality and treatment response of each patient.

unmet need (Nussbaum et al. 2015). While treatment of localized and newly diagnosed metastatic prostate cancer have seen tremendous strides in recent years with new androgen blocking agents, improved imaging, surgical, and radiation techniques, the number of men developing mCRPC is increasing (Scher et al. 2015). The incidence of mCRPC in the US is growing at roughly 1.7%/yr, estimated at 36,100 in 2009 and increasing to 42,970 in 2020 (Scher et al. 2015). With few treatment options, mCRPC patients continue to have markedly poor survival (13-30 months (Halabi et al. 2016)) and are in dire need of additional therapeutic options that overcome mechanisms of resistance. Current strategies such as androgen inhibition, chemotherapy (median survival 18-19 months) (Petrylak et al. 2004, Tannok et al. 2004), or T-cell therapy (Higano et al. 2009) offer only incremental benefit (median survival 26 months), but inevitably fail (Hotte et al. 2010). Patients failing first line chemotherapy survive only 12-16 months (Figure 1.3). While radiation is highly effective against prostate cancer, it cannot be delivered to widespread metastatic disease using conventional external beam techniques due to the toxicity of irradiating significant amounts of normal tissue. RPT offers a drastically different method of radiation delivery by linking a radioactive atom to a molecule targeting the tumor. This combined entity is injected, reaching all tumors. RPT unlocks new therapeutic potential but necessitates

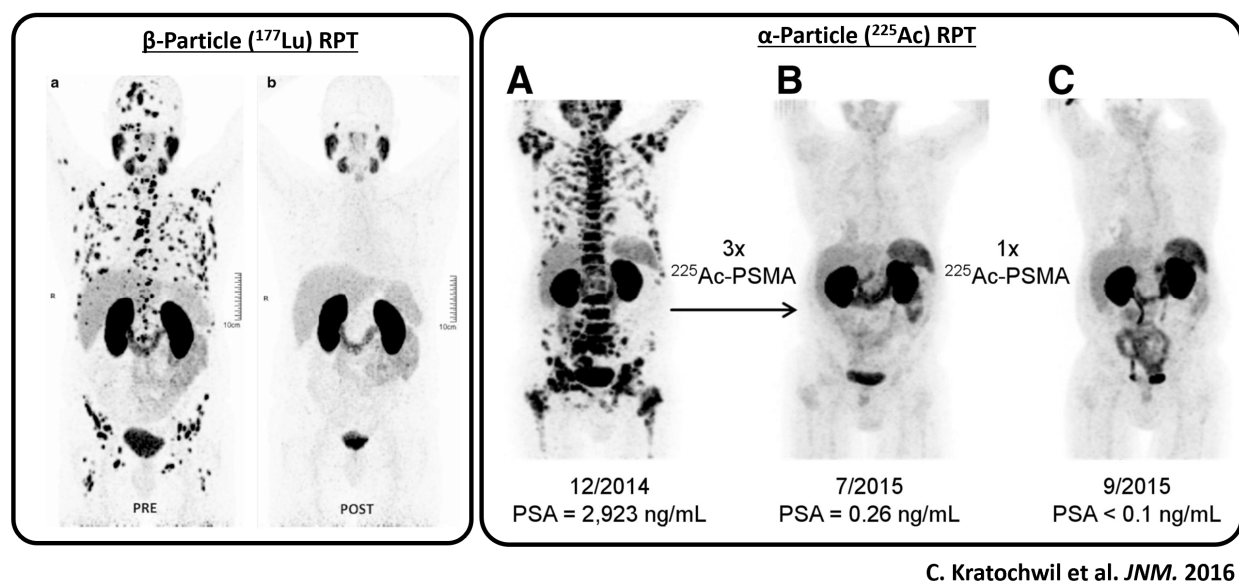


Figure 1.4: Promise of RPT as Seen in Literature. Figures from Kratochwil et al. 2016 that describe two patients that underwent either Lu-177 β -RPT or Ac-225 α -RPT. Both panels are scintigraphy images before and after RPT, with the dark spots present pre-therapy indicating tumors or pockets of metastatic disease. It is apparent that all of these metastatic sites disappear from the scintigraphy scan post-therapy.

accurate dosimetry for safe, effective personalization of therapy.

The promise of RPT is to deliver ablative radiotherapy to widespread metastatic disease. Molecularly targeted radiopharmaceutical therapy to PSMA (a ubiquitous (Kiehl et al. 2015) and specific tumor target in prostate cancer) offers a novel approach for mCRPC patients, but PSMA-targeted radiopharmaceutical therapy is ultimately limited by off-tumor toxicity caused by an inability to predict dose distribution *a priori*. The key to success of RPT is a relatively simple proposition: delivery of a high dose to the tumors and low dose to organs at risk (OARs). RPT using Lu-177 - a β emitter - is transforming prostate cancer (Kratowchwil et al. 2016), with the recent positive results of the VISION (Sartor et al. 2021) and TheraP (Horman et al. 2021, 2022) trials in metastatic patients showing survival benefits, and current trials underway in non-metastatic patients (Dhiantravan et al. 2021). α -based RPT has also shown promise in mCRPC patients, delivering an ultra-focal, highly effective radiation dose to prostate cancer cells, with clinical trials now being initiated. An example of its power is illustrated in the case report (Li et al. 2002) on 2 patients with mCRPC resistant to multiple lines of therapy (including 1 with β -emitting radiopharmaceuticals), treated with a PSMA-targeted α emitter, Ac-225, showing a remarkable response (Kratowchwil et al. 2016) (Figure 1.4). In an expanded study, 6 months after the delivery of anti-PSMA α therapy, 15/20 (75%) of the treated patients had a PSA decline, with 55% having a decline greater

than 80%.

Despite these promising results, most patients progress, indicating insufficient delivered dose. Complicating simple dose escalation, RPT can cause toxicity due to an inability to predict dose distribution *a priori*, and remains a major concern in mCRPC patients, who are heavily pre-treated. Treatment with RPT stands to be substantially improved with a better understanding of the variance in delivered tumor dose, treatment response, and survival to enable safe escalation of tumor dose and/or use with synergistic drug combinations (i.e., ICI, PARPi). Moreover, proper OAR constraints need further study, as the 23 Gy limit to the kidney, for example, may be too conservative, artificially limiting the dose delivered to the patient. Proper dosimetry data is also critical for evaluating newer agents using α emitters such as Actinium-225 (Ac-225), with 100-300X more energy deposited per cell per emission (Figure 1.4).

1.4 Need for Better Pre-Clinical *In Vivo* Dosimetry in RPT

These recent advances in the treatment of metastatic neuroendocrine cancers (Kratochwil et al. 2016, Kabasakal et al. 2017, McBean et al. 2019, Nautiyal et al. 2022, Sartor et al. 2021, Zang et al. 2019) have fostered significant interest in both optimizing RPTs for maximal therapeutic benefit – selectively targeting tumor tissue while avoiding OAR – and in extending these therapies to other cancers (Duan et al. 2022, Herrmann et al. 2022, Jadvar et al. 2018, Malcolm et al. 2019). Therefore, RPT development relies heavily on evaluating the uptake in both tumors and OARs *in pre-clinical models* to estimate RPT efficacy and select promising candidates for further study. We address this need by introducing a low-cost hand-held platform readily constructed in any laboratory setting for evaluation of RPT biokinetics *in vivo*.

RPT utilizes tumor-specific small molecules, antibodies, and derivatives thereof, conjugated to radioisotopes to systemically target cancer cells while sparing most normal tissues. Typically, the conjugated radioisotope is a β or α -emitter, that provides localized dose to the target lesions, with additional γ photon decay chains that are often used for imaging over the course of the therapy. RPT continually delivers dose over many days, and the dose delivered depends on tumor receptor expression level, ligand binding, retention, clearance, as well as radionuclide half-life, making measurement of delivered dose challenging. Moreover, dose to the non-target tissues depends on ligand circulatory half-life, clearance, and on-target but off-tumor binding. Despite the variability in both dose to the tumors and OARs due to these factors, a fixed dose is given to patients in clinical RPT administration resulting in significant patient-to-patient differences in total integrated dose delivered to tumors. Given the known dose response of tumors, this holds vital importance as subtherapeutic doses can lead to low treatment efficacy and early progression for many patients (Jadvar et al. 2018, Kratochwil et al. 2016, Malcolm et al. 2019, Sartor et al. 2021). The critical goal of RPT

is to escalate and maximize tumor dose while minimizing dose deposition and the resultant toxicity to OARs (Duan et al. 2022, Jadvar et al. 2018, Malcolm et al. 2019), necessitating a precise understanding of total integrated dose and its variance during pre-clinical evaluation. This type of data can allow for movement from a traditional single-shot therapy approach to an adaptive therapy approach, in order to decrease/prevent therapeutic resistance and improve treatment response (Figure 1.5). This type of pre-clinical data is currently not available using existing, commonly accessible laboratory methods due to lack of temporal resolution (Carpanese et al. 2024, Ling et al. 2020, Moroz et al. 2020, Pienta 2008) and/or discontinuity of data over the entire biodistribution curve (Bartoli et al. 2022, Houghton et al. 2017, Keidar et al. 2017, Khosravifarsani et al. 2022, Kruijff et al. 2019, Satterlee et al. 2015, Stuparu et al. 2020, Qin et al. 2020).

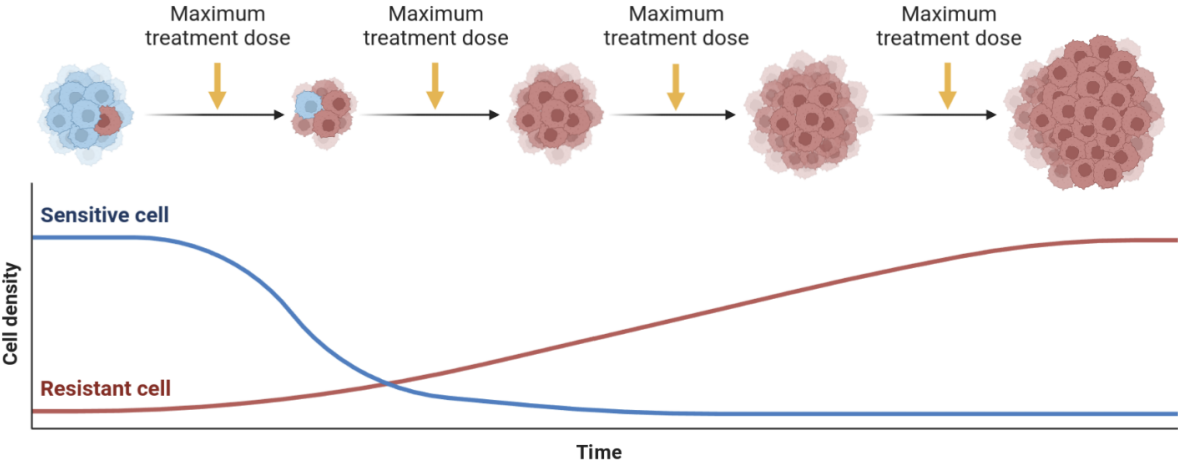
1.5 State-of-Art in Pre-Clinical *In Vivo* Dosimetry

Currently, pre-clinical studies of RPT biodistribution are evaluated using small animal single photon emission computed tomography (SPECT) and/or *ex vivo* γ counting. SPECT/CT provides a whole animal snapshot at a single time point, and this is often repeated every few hours to create a sparse chronic binding kinetics curve. Since small animal SPECT/CT acquisitions require sufficient counts to increase image signal-to-noise (SNR) ratio, acquisitions are usually on the order of 30 minutes to 1 hour. This low temporal resolution loses information regarding initial binding kinetics, which can change on the order of minutes, and corresponds to the time when the maximum dose is administered to OAR and significant dose is administered to tumors. In addition, small animal SPECT/CT machines are costly and not widely available, which hinders the ability to study this promising therapeutic modality across labs and in resource-limited environments.

Another approach is *ex vivo* γ counting that involves taking a sample of the tumor or OAR, and quantifying the γ activity of the sample, which is then used to extrapolate the activity of the whole tumor or OAR at the time the animal model was euthanized. This method is more sensitive than SPECT to γ emissions, making it the primary mode of dosimetry for many radiopharmaceutical studies that require high sensitivity, like α -based RPT. Since the *in vivo* models are euthanized after each time point of interest, there is often significant variability from model-to-model. Moreover, instead of averaging out the heterogeneity, it may be useful to monitor the kinetics of each pre-clinical model, in order to more completely understand the variance in biodistribution of the RPT under evaluation – information that is lost using *ex vivo* dosimetry.

To address these requirements, we present a scalable optical fiber-based γ sensitive biosensor platform (Figure 1.6(d)) and workflow for pre-clinical evaluation of radiopharmaceutical uptake in tumors and OARs (Lall et al. 2022, 2023). These probes share the same detection, counting, and acquisition circuitry, allowing the system to easily scale the number of biosensors to many tumors and OARs by utilizing additional optical fibers. Compared to commercial γ laparoscopic probes (Devicor Medical Products 2023, Lightpoint Medical

Traditional therapy



Adaptive therapy

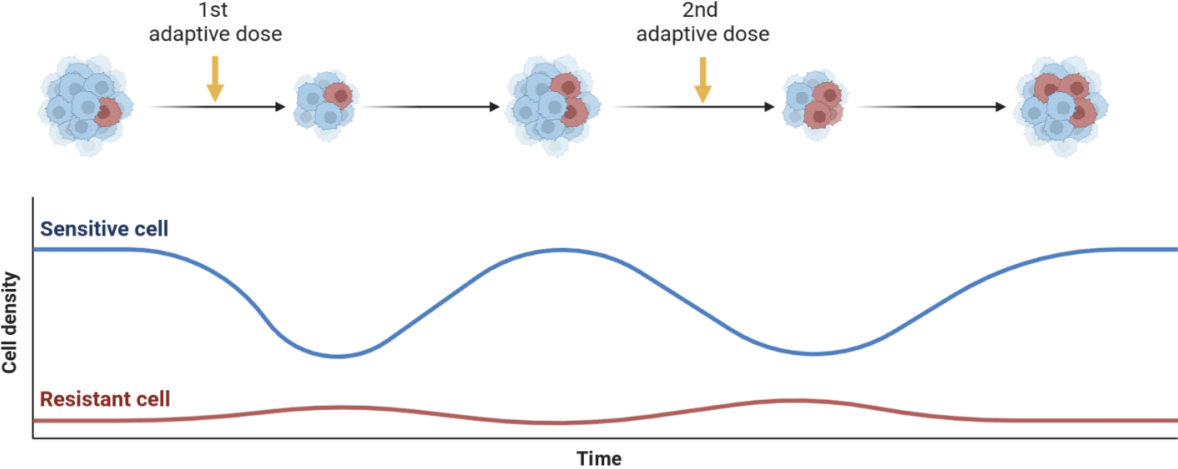


Figure 1.5: Optimizing Cancer Radiotherapy in a Patient-Specific Manner. Due to the heterogeneity in the clinical presentation of cancer and the fact that many patients become resistant to certain types of therapy (anti-androgen hormone therapy, chemotherapy, etc.), cancer therapy is moving away from traditional single dosing to adaptive personalized dosing for every patient. This helps prevent proliferation of resistant cells, improve treatment delivery to target cells, and reduce toxicity.

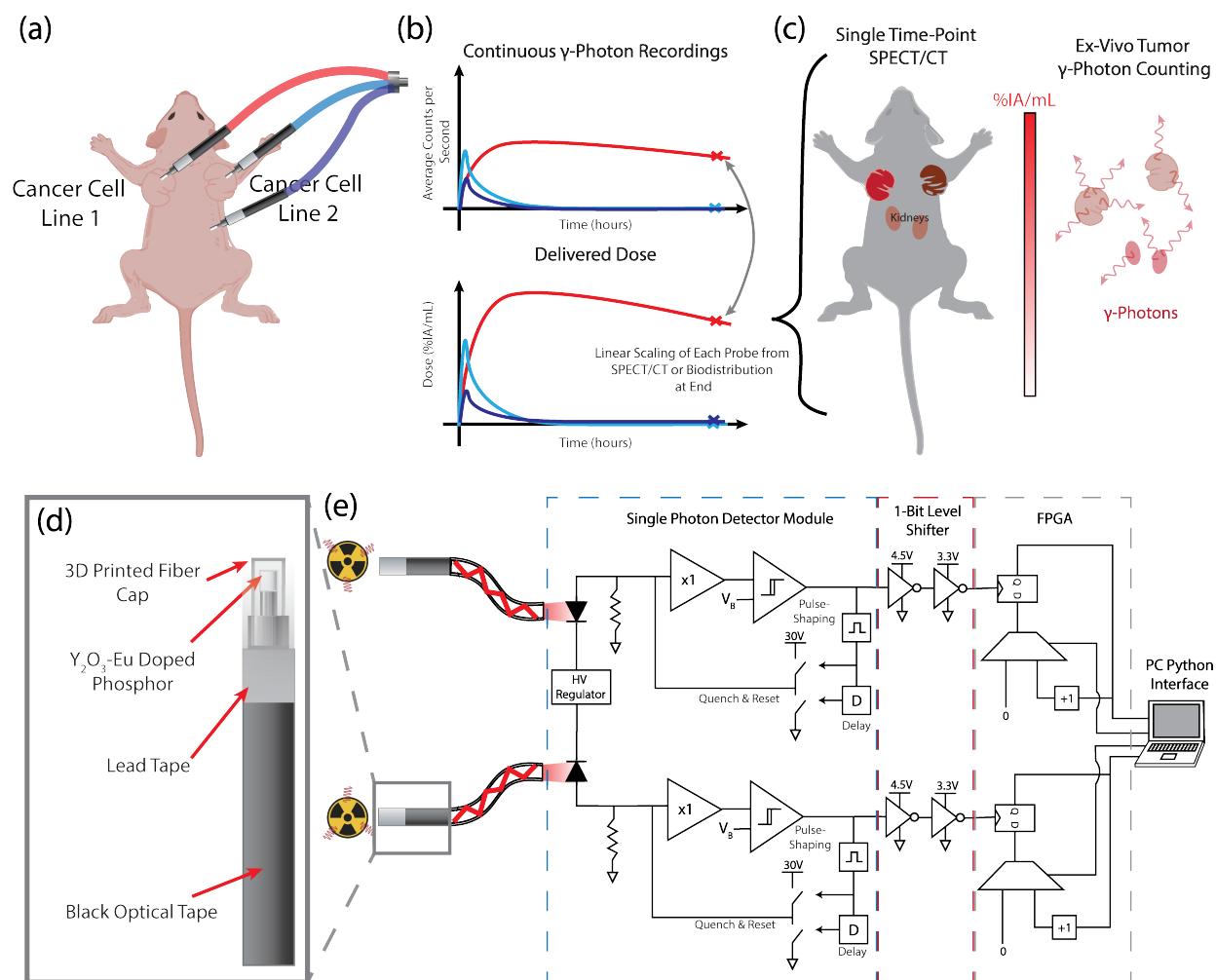


Figure 1.6: Conceptual Workflow and Optical Fiber γ -Photon Biosensor Design. (a) An *in vivo* model with two tumors from different cancer cell lines is administered a RPT and (b) measured using the proposed γ biosensor platform at very fine intervals with short acquisition times. (c) At the last time point, a single SPECT/CT or *ex vivo* γ counting is done to convert the γ counts from the biosensor to %IA/mL. (d) Optical sensing front end with compacted Y_2O_3 -Eu doped phosphor at face of optical fiber that is surrounded with lead tape and optical tape. (e) Optical fiber is interfaced to readout circuitry, including APDs, amplifiers, level-shifters, digital counters, and data readout.

2023), MOSFET dosimeters (Beyer et al. 2008, Gulp et al. 2009), calorimetric dosimeters (Kim et al. 2022, Tregubov et al. 2022), luminescence imaging (Bhatt et al. 2018, Zhang et al. 2020, Balkin et al. 2014), and other scintillator-based approaches (Zhang et al. 2021), this custom set of biosensors has similar or better sensitivity with a smaller detector area and enables multiplexed sensing, allowing for many small tumors and organs to be simultaneously monitored in *in vivo* models with a smaller acquisition time. In practice, short acquisitions with the biosensor would be taken at finely swept time points to provide continuous, real-time γ count data over the course of the therapy (Figure 1.6(a)). After the last probe measurement has been completed for the final time point of interest, either a single SPECT/CT scan or *ex vivo* γ counting can be conducted immediately afterwards (Figure 1.6(c)). This allows for the derivation of the linear scaling factors between counts per second (CPS) from each probe and radiation dose expressed as percent injected activity per mL of tissue (%IA/mL) in the tumor or organ of interest (Figure 1.6(b)).

We show the utility of the developed system and validate it for use in pre-clinical evaluation by (1) performing a dilution of Lu-177-PSMA-617 (FDA-approved treatment for metastatic castration resistant prostate cancer) in the pre-clinically relevant activity range (0.5 - 500 $\mu\text{Ci/mL}$) and measuring the γ counts outside of each vial to show the system's high sensitivity and linear dynamic range with radiopharmaceutical activity, (2) collecting real-time data outside prostate cancer PC3-pip and PC3-flu tumors in 15 mouse models administered Lu-177-PSMA-617 RPT and showing how real-time trends and variance in uptake, rate of uptake or excretion, and therapeutic ratio can be captured with our platform, (3) showing the linear relationship between the average γ counts per second from our biosensor with the activity/mL of tissue from both SPECT/CT and *ex vivo* dosimetry of the 15 mice, and (4) demonstrating the intended use case of the system by measuring both tumor and OAR activity in a single mouse model over time and showing that the biosensor's γ counts are consistent with SPECT/CT.

Chapter 2

Design of Optical Fiber-Based γ Photon Biosensor

2.1 Design Overview

Y_2O_3 -Eu doped phosphor (Sigma Aldrich, 756490) was coupled to the face of an optical fiber patch cable (THORLABS, M104L01) and used to scintillate incoming γ 's into 610 nm red light, compatible with peak solid-state photon detection. 0.25 g of phosphor was compacted to an optimized thickness of 500 μm (Fig. 2.1), to eliminate air gaps and increase density, and hence the mass attenuation coefficient (NIST 2023). The high light-to-light quantum efficiency, customizable form factor, and low cost of the Y_2O_3 Eu-doped phosphor enables use of only a thin (500 μm) and low detection surface area (4.9 mm^2) layer of the phosphor to scintillate incoming γ -photons effectively. This is in contrast to state-of-art nuclear medicine γ -sensing instrumentation where scintillators are multiple centimeters thick (O'Keeffe et al. 2015, Woulfe et al. 2016, Zhang et al. 2021), leading to low specificity, large size, low maneuverability, and increased system cost.

Because patch cables are very light sensitive, five layers (500 μm) of black optical tape (THORLABS T743-2.0) were placed on the outside of the fiber throughout its length to ensure no ambient light photons were mistaken as γ -photon events (Figure 2.3). Probes were surrounded with 1 mm of lead tape to prevent measurement of γ counts from organs adjacent to the one of interest. The fibers were optically coupled to silicon avalanche photodiodes (APD) to detect the scintillation photons. The customized γ sensitive optical fiber-based sensor is shown in Figure 1.6(d). The APDs (Excelitas, SPCM-AQ4C) have a circular active area of 180 μm and peak photon detection efficiency of 60% at 650 nm. They are biased above their breakdown voltage, such that single 610 nm photons will trigger an avalanche response at the diode sensing node and thereby be sensed. This voltage is fed into a unity gain buffer and sensed by a comparator to create a 25 ns wide, rail-to-rail voltage pulse. The APD is subsequently quenched and the diode is reset by lowering the bias voltage below breakdown. In this state, the APD is not single-photon sensitive, which leads to a dead time

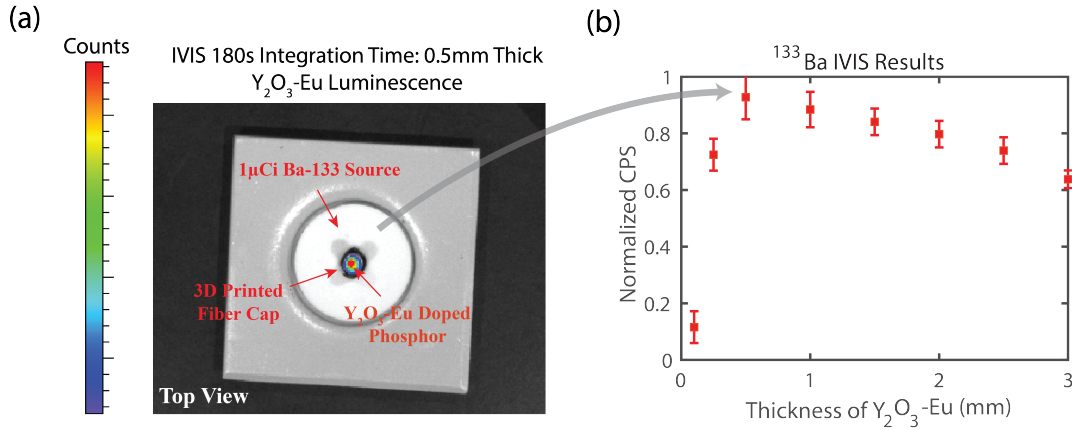


Figure 2.1: Optimizing Scintillating Phosphor Thickness for Desired Sensitivity and Dynamic Range (a) IVIS image generated (with an 180 s integration time) of ^{133}Ba point source planted on disk with 3D printed fiber cap containing optimized $500\mu\text{m}$ thick $\text{Y}_2\text{O}_3 - \text{Eu}$ doped phosphor. This was repeated for 8 different thicknesses. (b) Normalized total counts from IVIS versus scintillator thickness over a 180 s integration time.

of 50 ns. Given this 25 ns wide digital pulse and 50 ns dead-time, the system can theoretically be operated in an environment with a maximum flux in the megacounts/sec range before seeing significant nonlinear effects due to dead-time. The scintillator surface area and optical fiber aperture diameter was chosen such that the system operates well below this maximum flux threshold to prevent dead-time effects and decrease dynamic power consumption during system operation. This also allows for ease in extending to other radiotherapy applications by simply scaling the surface area of the phosphor, depending on the range of expected gamma-photon flux. The comparator outputs 4.5 V square pulses which are subsequently level shifted (TI SN74LVC1G14) to 3.3V, the logic level of the field programmable gate array (FPGA, Opal Kelly XEM6010) that was used. These pulses, each representing an incoming scintillated photon, are then counted using digital counters implemented on the FPGA (Verilog synthesized using Xilinx ISE). The FPGA sends data to the PC via a serial link and automated Python interface (developed with Opal Kelly python API libraries) at 42 MHz to allow for continuous and multiplexed data relay of scintillated counts per second (CPS), which is proportional to the γ flux (Figure 1.6(e)).

2.2 γ -Photon Scintillator

Thickness Optimization

The phosphor thickness was optimized by measuring the total number of visible light photons emitted in response to a $1\mu\text{Ci}$ encapsulated ^{133}Ba point source, while sweeping eight

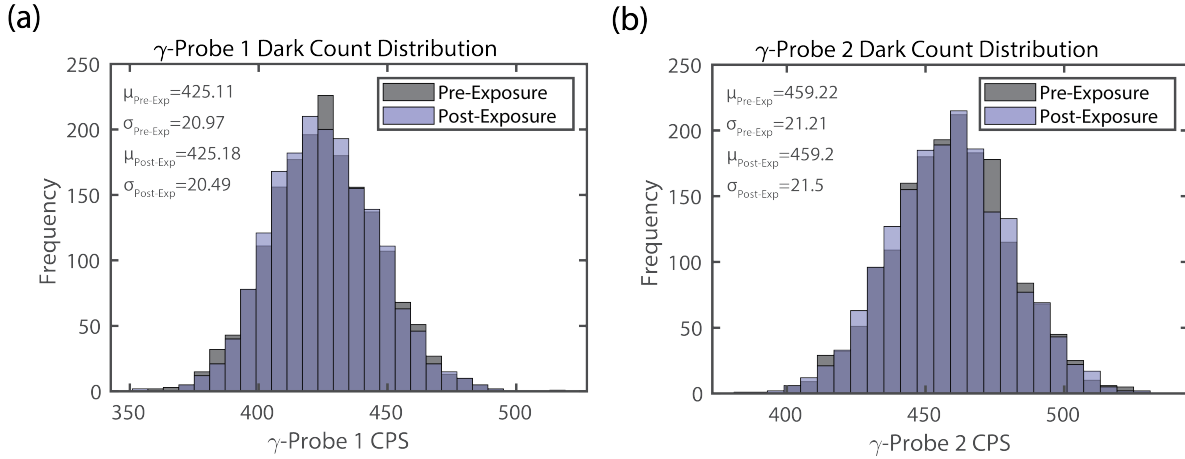


Figure 2.2: Measuring Scintillator Afterglow. Dark count of each APD before a full serial dilution experiment with 10 minute exposure per vial vs. dark count after the full serial dilution experiment for (a) probe 1 and (b) probe 2 used for the *in vivo* experiments.

thickness values between $100 \mu\text{m}$ and 3 mm to evaluate the tradeoff between mass attenuation coefficient and self-absorption of the emitted 610 nm red light. A 3D printed fiber cap was placed directly on top of the ^{133}Ba encapsulated point source, and was placed into a Xenogen IVIS 50 Imaging System. The thickness of phosphor present in the fiber cap was incrementally changed and the total counts were recorded over a 180 s integration time (Figure 2.1(a)). The results of this sweep can be seen in Figure 2.1(b), with the optimum of the tested values found to be a thickness of approximately $500 \mu\text{m}$.

Scintillator Afterglow

Afterglow effects, the fraction of scintillation light still present for a certain time after a radioactive source is removed, for the phosphor were studied by measuring the dark count distribution that occurs intrinsically from each of the APDs used. The dark count distribution before and after a full serial dilution exposure of 11 radioactive vials, starting with $0.5 \mu\text{Ci}$ and ending with $500 \mu\text{Ci}$ in 2x steps was measured. The dark count before the full serial dilution was measured for 30 minutes. The 30 minutes immediately following the full serial dilution acquisition were also measured (Figure 2.2). No significant scintillator afterglow effects were observed in this system, with the dark count distribution before and after exposure being nearly identical.

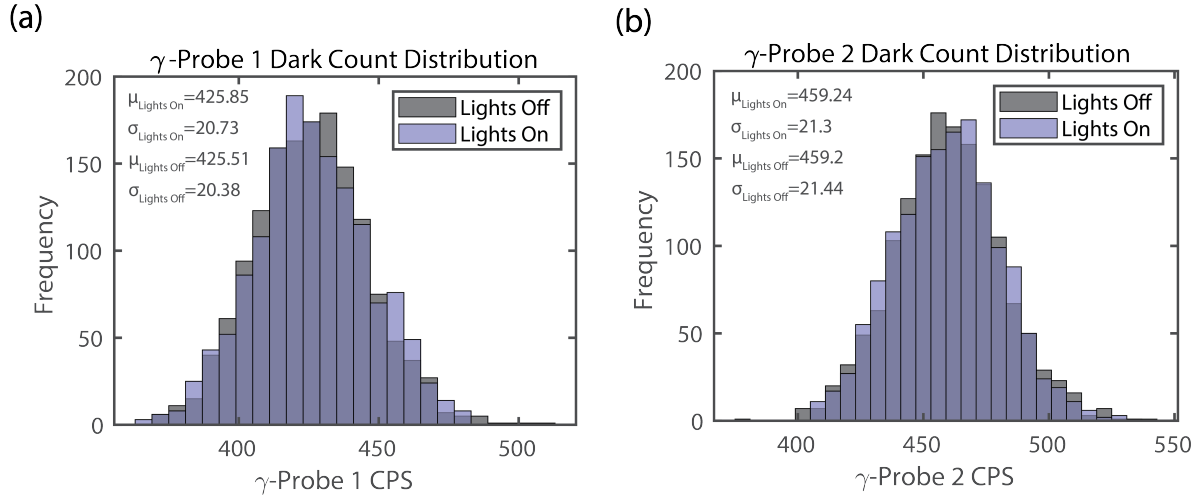


Figure 2.3: Visible Light Shielding of Optical-Fiber Biosensor Dark count of each APD in a light-sealed box vs. in a well lit room for (a) probe 1 and (b) probe 2 used for the in vivo experiments.

2.3 Visible Light Shielding

Optical fiber patch cables were chosen due to their low insertion loss and hence their ability to deliver scintillated photons efficiently over long lengths. The trade-off is that patch cables are normally very visible light sensitive to their ambient environment as well. To mitigate this, five layers (500 μm) of black optical tape were placed on the outside of the fiber throughout its length to ensure no ambient light photons were mistaken as γ -photon scintillation events. Each layer of the black optical tape was characterized to have an optical density (OD) of 4, allowing only 0.01% of light incident on it through. With the five layers, the probability of detection of incident light intensity becomes 1×10^{-20} . To ensure sufficient visible light shielding from varying environmental conditions, counts were measured over a three hour period from each γ -probe in a well-lit room and in a light-tight box and compared, with no visible light photon counts recorded in either case (Figure 2.3). This ensures that only γ -photons are being sensed.

2.4 Characterization of γ -Photon Biosensor

To characterize the sensor’s response to a γ -emitting radionuclide, a serial dilution of conjugated Lu-177-PSMA-617 was performed using saline. 11 eppendorf tubes were prepared by performing a 2x dilution of activities varying between 0.5 μCi and 500 μCi in 1 mL (the physiologically relevant activity range of *in vivo* RPT). The eppendorf tube was placed in a 3D printed stand with each γ -probe placed on the outside surface of the vial. Detector

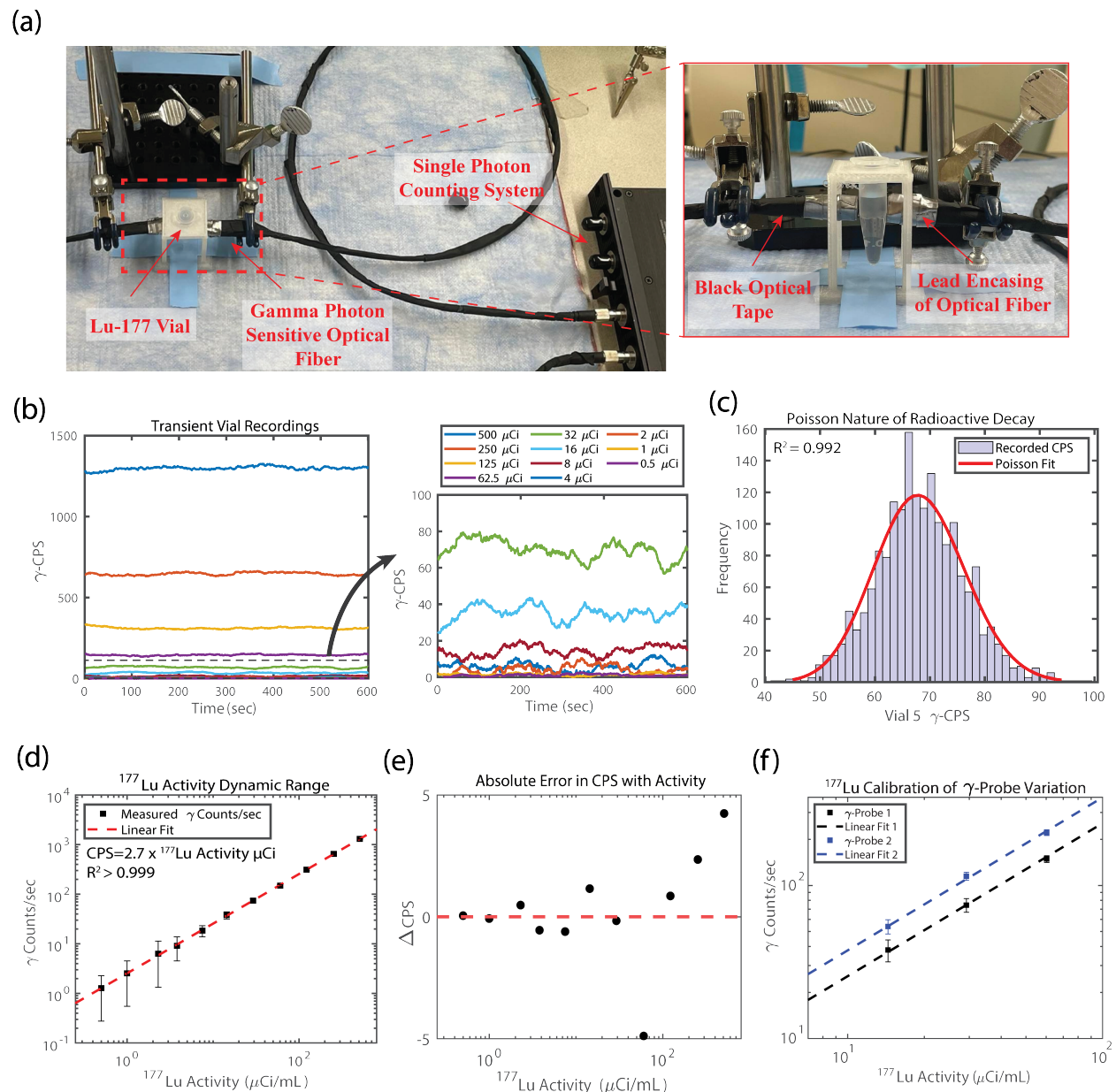


Figure 2.4: Characterization of Optical Fiber Biosensor with Lu-177 Activity (a) Lu-177 serial dilution experimental setup. (b) Lu-177 serial dilution real-time transient results of γ CPS with activities ranging from 0.5 to 500 $\mu\text{Ci/mL}$. (c) Poisson fit of recorded γ CPS distribution, as count variation can be attributed to the Poisson nature of radioactive decay. (d) Average CPS from the proposed system is highly linear with activity, for activities ranging from 0.5 μCi to 500 μCi . (e) The absolute error in CPS for the activity range of interest (f) Sensitivity calibration of the two biosensors that were used for the majority of this study, using the setup in (c) as well

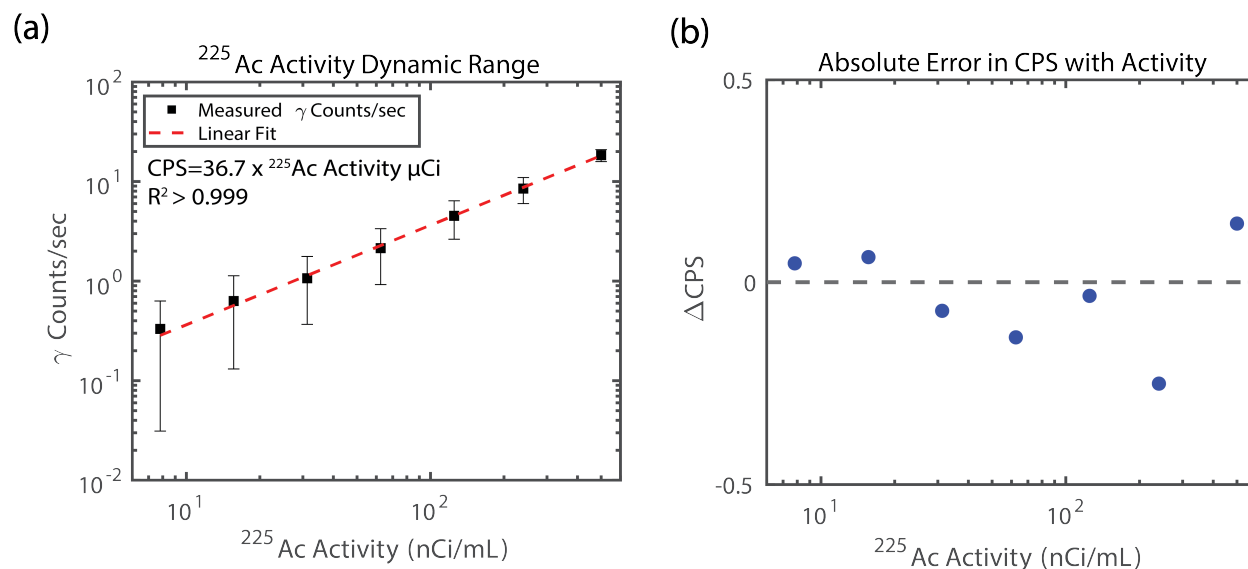


Figure 2.5: Characterization of Optical Fiber Biosensor with Ac-225 Activity Measured CPS from outside of a Ac-225 2x dilution with the proposed system. Each vial was measured for 30 minutes. (a) Average CPS from the proposed system is highly linear with ^{225}Ac activity, for activities ranging from 7.8 nCi to 500 nCi in 1 mL. (b) The absolute error in CPS for the activity range of interest.

position was held constant and vials were incrementally changed (Figure 2.4(a)). γ CPS were recorded for 10 minutes. The linear fit to the serial dilution data was fit using the least-squares solution with no intercept. The sensors demonstrated high linear dynamic range with counts ranging from 1.2 to 1,306 CPS for Lu-177 activities ranging from 0.5 to 500 $\mu\text{Ci}/\text{mL}$ respectively (Figure 2.4(b)), with an R^2 value of 0.9998 (Figure 2.4(d)). Dead-time of the device and FPGA counting system, detector sensing and readout circuit noise, sensor hysteresis, and scintillator afterglow (Figure 2.2) were insignificant and had no effect on sensor accuracy and sensitivity at the tested therapeutic doses of Lu-177-PSMA-617 therapy, in contrast to many other γ counting (Beyer et al. 2008, Gulp et al. 2009, O’Keeffe 2015, Woulfe et al. 2016, Zhuang et al. 2016) and CCD camera (Bhatt et al. 2018, Zhang et al. 2020, Balkin et al. 2014) based techniques. Absolute error in CPS between the least-squares linear regression fit and the acquired data ranged up to 5 CPS in magnitude (Figure 2.4(e)), with a mean error of 0.26 CPS and standard deviation in error of 2.2 CPS. Most of the uncertainty in CPS with Lu-177 activity is due to the Poisson nature of radioactive decay. Figure 2.4(c) shows an accurate ($R^2=0.992$) Poisson fit of the recorded CPS distribution from the 32 μCi vial reading, and any noise generated by the detector is below this variation. A similar dilution was performed with Ac-225 over physiologically relevant concentrations (7.8-500 nCi/mL). The serial dilution performed with Ac-225 (Figure 2.5) had a similar linear

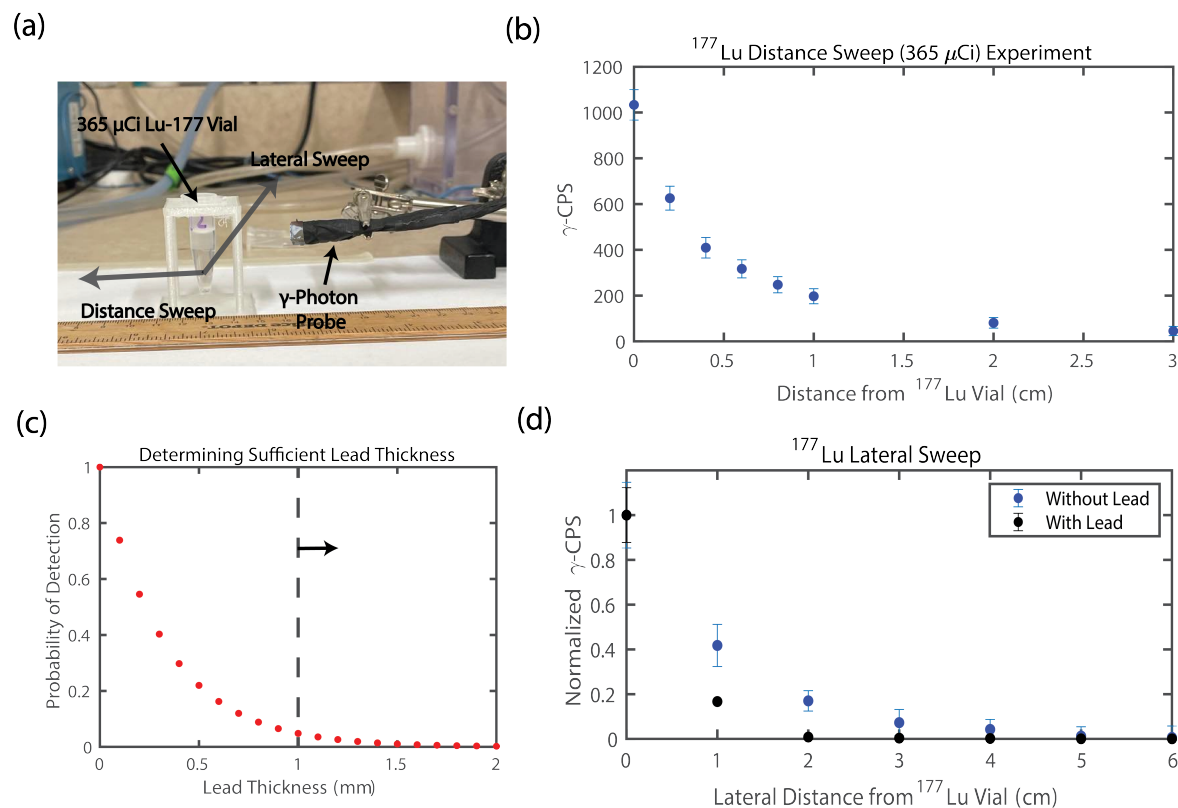


Figure 2.6: Design of Lead Shielding to Mitigate Organ-to-Organ Cross-Talk (a) Experimental setup to test the developed system’s transfer function with distance and to test if the lead thickness was sufficient to prevent cross-talk of recorded gamma CPS. A 365 μCi Lu-177 vial was swept from 0 to 3 cm away from the sensor face as well as 0 to 6 cm laterally. (b) Transfer function between recorded γ CPS and distance away from the sensor face. (c) Probability of detection for the weighted average energy γ photon from Lu-177 for various thicknesses of lead. (d) Measurement of lateral distance transfer function with and without 1 mm thick lead tape.

response over this concentration range with an R^2 value of 0.999.

Because there is some variation in sensitivity between the two probes, a three point calibration was done where three vials with varying activities of Lu-177-PSMA-617 (15 μCi , 30 μCi , 60 μCi) were diluted with saline and were measured by each probe flush against the vial. The linear relationship between CPS and Lu-177-PSMA-617 activity was created for each probe using the three vials (Figure 2.4(f)). The slope of the best fit lines were compared to find the factor difference in sensitivity between them in order to correctly compare data.

2.5 Distance Transfer Function Derivation

Since *in vivo* tumors are typically bounded by 1 cm^3 , an eppendorf vial of 1mL, 365 μCi of Lu-177-PSMA-617 was used as the γ -emitting source to characterize angular and distance dependence of the sensing probe. The vial was placed in a 3D printed vial holder and the γ -sensing probe was placed flush against the surface of the vial. Detector position was held constant, and the 3D printed stand was incrementally moved away from the sensing probe. 8 distances between 0 and 3 cm away from the outside surface of the vial were tested (Figure 2.6(a),(b)).

2.6 Lead Shielding

Since uptake of other tumors and OAR in the *in vivo* model can cause cross-talk of γ CPS and result in inaccuracy in the mapped back activity, some lead shielding around the fiber was necessary. To attain a sufficient mass attenuation coefficient for the Lu-177 γ photon energies of interest (predominantly 208 keV, 113 keV), at least 1 mm thick lead needed to be used around the periphery of the scintillating phosphor area. The efficacy of this lead shielding was tested by placing a 1 mL, 365 μCi vial of Lu-177-PSMA-617 in a 3D printed stand, 1 cm away from the face of the sensing probe. The vial was incrementally moved laterally in plane with the sensor face at 7 distances between 0 and 6 cm. This experiment was conducted with and without the 1 mm thick lead tape around the fiber periphery (Figure 2.6(c),(d)).

Chapter 3

Applying the Optical Fiber-Based Biosensor *In Vivo*

3.1 *In Vivo* Mice Experimental Procedures

The γ biosensors were assessed on 16 *in vivo* prostate cancer murine models to demonstrate the linear mapping of the biosensor signal to tumor activity. Mice were housed in a pathogen-free environment under protocols approved by the UCSF Institution of Animal Care and Use Committee. The system was evaluated for monitoring *in vivo* binding kinetics by utilizing mouse models bearing two human prostate cancer cell lines on their flanks. PC3-pip (PSMA+) and PC3-flu (PSMA-) tumor cells were subcutaneously (SQ) injected into the left and right flanks respectively of 16 (M1-M16) male athymic nude mice (Figure 3.1(a)). PC3-pip and PC3-flu tumors model tumors with high PSMA expression and OARs with low PSMA expression, respectively. After 2 weeks, the tumor size reached approximately 1 cm in its major axis allowing for a suitable dose integration volume on SPECT for accurate comparison to the proposed system. Mice were subsequently administered approximately 600 μCi of Lu-177-PSMA-617 via tail vein injection (Fig. 3.1(b)).

To validate the probe measurements at various points along the biodistribution curve, each of mice M1-M15 was measured under light anesthesia with the system for 2 hours at one of five time points post-injection: 0 hr (M1-M3), 6 hr (M4-M6), 12 hr (M7-M9), 24 hr (M10-M12), and 48 hr (M13-M15). Three mice were measured at each time point to allow for statistical analysis. During each measurement interval, one γ -photon probe was placed on each tumor of the mouse: one on the PC3-pip tumor and the other on the PC3-flu tumor. γ -photon probes were placed in such a way to prevent crosstalk, i.e. the probe from the PC3-flu tumor measuring the counts from the PC3-pip tumor and vice versa (Figure 3.1(c)). After each 2-hour acquisition, M1-M15 were euthanized, and a SPECT/CT was taken immediately afterwards (Figure 3.1(d)). The tumors were then dissected to perform *ex vivo* γ counting (Figure 3.1(e)). In contrast, mouse M16 was chronically monitored from 0 to 48 hours post injection (h.p.i.) with one probe on each tumor as with M1-M15, but

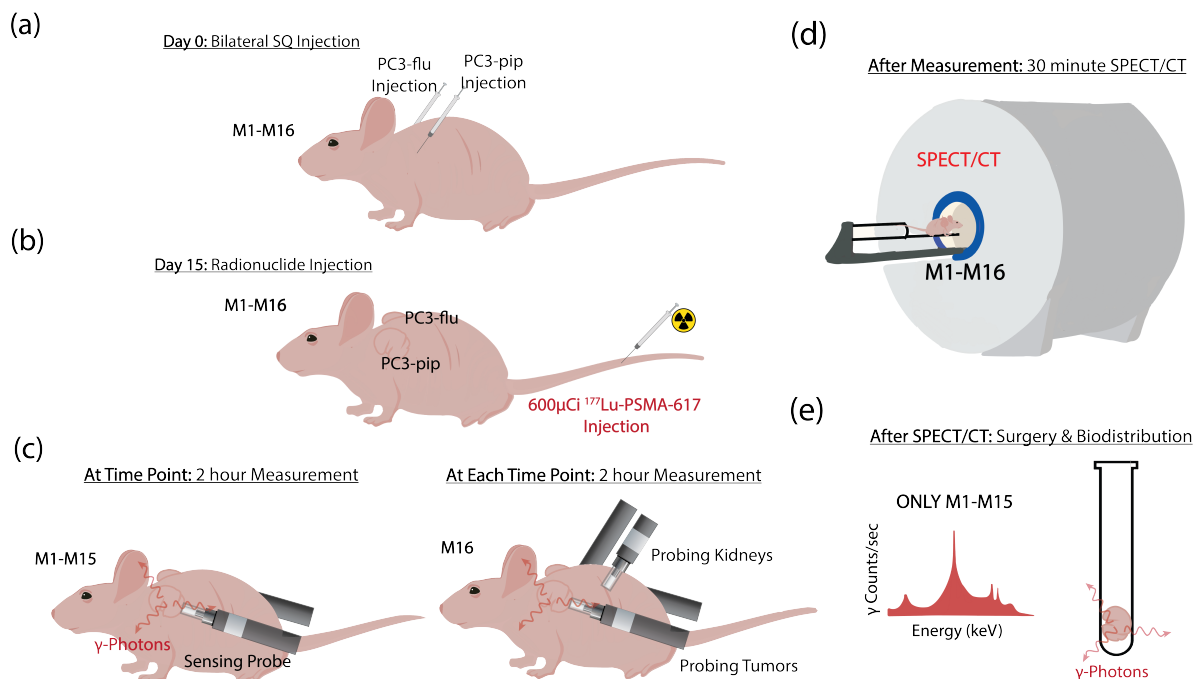


Figure 3.1: *In Vivo* Experimental Setup. (a) SQ injection of PC3-pip and PC3-flu cells into flanks of mice M1-M16. (b) After 14 days, the two tumors grew to be palpable and $600\mu\text{Ci}$ of Lu-177-PSMA-617 was administered to mice M1-M16 via tail-vein injection. (c) One γ biosensor is placed behind each tumor in mice M1-M16, while under anesthesia for 2 hours. M1-M15 are monitored at a single time point post injection, but M16 is chronically monitored over five timepoints post-injection. M16 also has two additional probes placed vertically above the left and right kidneys to track kidney (OAR) uptake and clearance. (d) Immediately after their respective 2-hour measurement, mouse M1-M15 are euthanized and a SPECT/CT is taken. M16 is not euthanized and is chronically monitored, with a SPECT/CT taken after each γ biosensor acquisition. (e) The tumors of mice M1-M15 are dissected, and a small sample of the tumor is used to perform *ex vivo* dosimetry.

also with an additional probe hovering over each kidney (Figure 3.1(c)). M16 was measured continuously under light anesthesia for 2 hours at each of the 5 time points (0, 6, 12, 24, 48 h.p.i.). After each γ probe acquisition, a SPECT/CT was taken of M16 (Figure 3.1(d)) for comparison.

3.2 Radiolabelling of $^{177}\text{Lu-PSMA-617}$

$^{177}\text{LuCl}_3$ was purchased from Oak Ridge National Laboratory. In dimethyl sulfoxide (DMSO), a stock solution of PSMA-617 (Vipivotide tetraxetan, MedChemExpress) is made at a con-

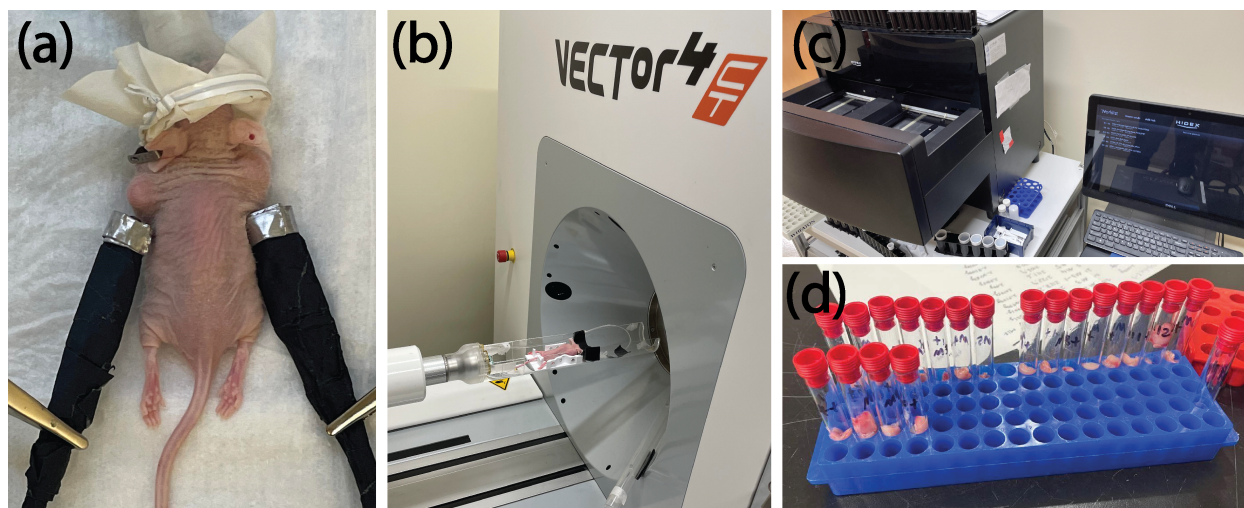


Figure 3.2: Implemented *In Vivo* Experimental Setup. (a) Athymic nude mouse (M1-M15) with bilateral tumors (PC3-pip, PC3-flu). Each tumor was monitored with the proposed γ biosensor for 2 hours at a specific time point post-injection. M16 has the same experimental setup but with 2 additional γ biosensors on each kidney. (b) Small-animal SPECT/CT machine used to perform state-of-art imaging based dosimetry. (c) HIDEX biodistribution machine used for state-of-art *ex vivo* dosimetry. (d) The tumors of mice M1-M15 are dissected after the SPECT/CT scan, and a small sample of each tumor is placed in individual vials to perform *ex vivo* dosimetry.

centration of 1 mg/mL. Transferring 9 mCi of $^{177}\text{LuCl}_3$ to a reaction vial, 100 μL of 0.2M ammonium acetate was used to bring the pH of the solution down to 6. After adding 25 μg of PSMA-617 to the vial, the reaction is allowed to happen at 50°C with continuous shaking for 45 minutes. Then, to assess labeling effectiveness, thin layer chromatography (TLC) was carried out using Whatman 41 paper as the stationary phase, 20 mM citric acid as the mobile phase, and an AR-2000 Bioscan TLC Reader.

A SEP-PAK Plus C8 cartridge that has been preconditioned with 5 mL of 100% ethanol and 5 mL of water is used to purify ^{177}Lu -PSMA-617. The waste solution (unlabeled ^{177}Lu) is collected in a vial after the reaction solution has been forced through the cartridge. 2 mL of 100% ethanol solution is used to elute ^{177}Lu -PSMA-617, and then the ethanol is evaporated under vacuum while being continuously flushed with N_2 at 40°C. Before preparing the mice injections, dried ^{177}Lu -PSMA-617 is reconstituted in a solution of DMSO:Tween 80:saline (10%:10%:80% volume per volume). I would like to acknowledge Dr. Shalini Chopra at UCSF for her knowledge and assistance in radiolabelling ^{177}Lu -PSMA-617.

3.3 SPECT/CT Acquisitions

The SPECT/CT (VECTor4CT, MILabs) utilized a high-energy multi-pinhole collimator (HE-GP-RM) and was taken with a 30 minute SPECT acquisition with an energy detection range of 0-1.2 MeV. This was followed by a CT scan with a tube current of 0.19 mA, tube voltage of 55 kVp.

3.4 *Ex Vivo* Biodistribution

Small portions of the PC3-pip and PC3-flu tumors were dissected from each mouse. Small slices of each tumor were placed in test tubes and loaded into a HIDEX automatic γ -counter that was used to quantify the activity from each of the tumors. Removal of only a small tumor section prevents the saturation of γ -counting and avoids inaccuracy in measured activity.

Chapter 4

Tracking Real-Time Tumor Binding Kinetics in *In Vivo* Models

4.1 Visualizing Real-Time Tumor Binding Kinetics

The ability to monitor changes in *in vivo* RPT uptake, excretion rates, and therapeutic ratio, was demonstrated in M1-M15. The real-time transient trends in tumor uptake for M1-M15 are shown in Figure 4.1. Figure 4.1(a) shows a representative SPECT/CT scan of one mouse from each of the five time points (M1, M4, M7, M10, M13), with that mouse's biosensor transient plots for both the PC3-pip and PC3-flu tumors shown in Figure 4.1(b). All transient plots show the average CPS for a 1-minute recording, over the 2-hour recording period. M1's (0-2 h.p.i) transient plot shows the CPS in both PSMA+ (PC3-pip) and PSMA- (PC3-flu) tumors increasing rapidly, reflective of the initial biodistribution of ^{177}Lu -PSMA-617 in the bloodstream. Shortly after injection, the CPS from both tumors began to increase with preferential binding to the PSMA+ PC3-pip tumor occurring almost immediately. The CPS for both tumors peaked at around 5 minutes and then slowly began to fall reflecting radiopharmaceutical clearance from the blood. The PC3-flu tumor's CPS decreased much faster than the PC3-pip and settled to a lower value after 2 hours. This indicates increased binding and retention in the PC3-pip tumor and increased clearance but still non-negligible off-target uptake by the PC3-flu tumor (reflective of an OAR). M4's (6-8 h.p.i), M7's (12-14 h.p.i), M10's (24-26 h.p.i), and M13's (48-50 h.p.i) transient plots all show progressively increasing separation between the CPS from the PC3-pip and PC3-flu tumors over the 2-hour recording times.

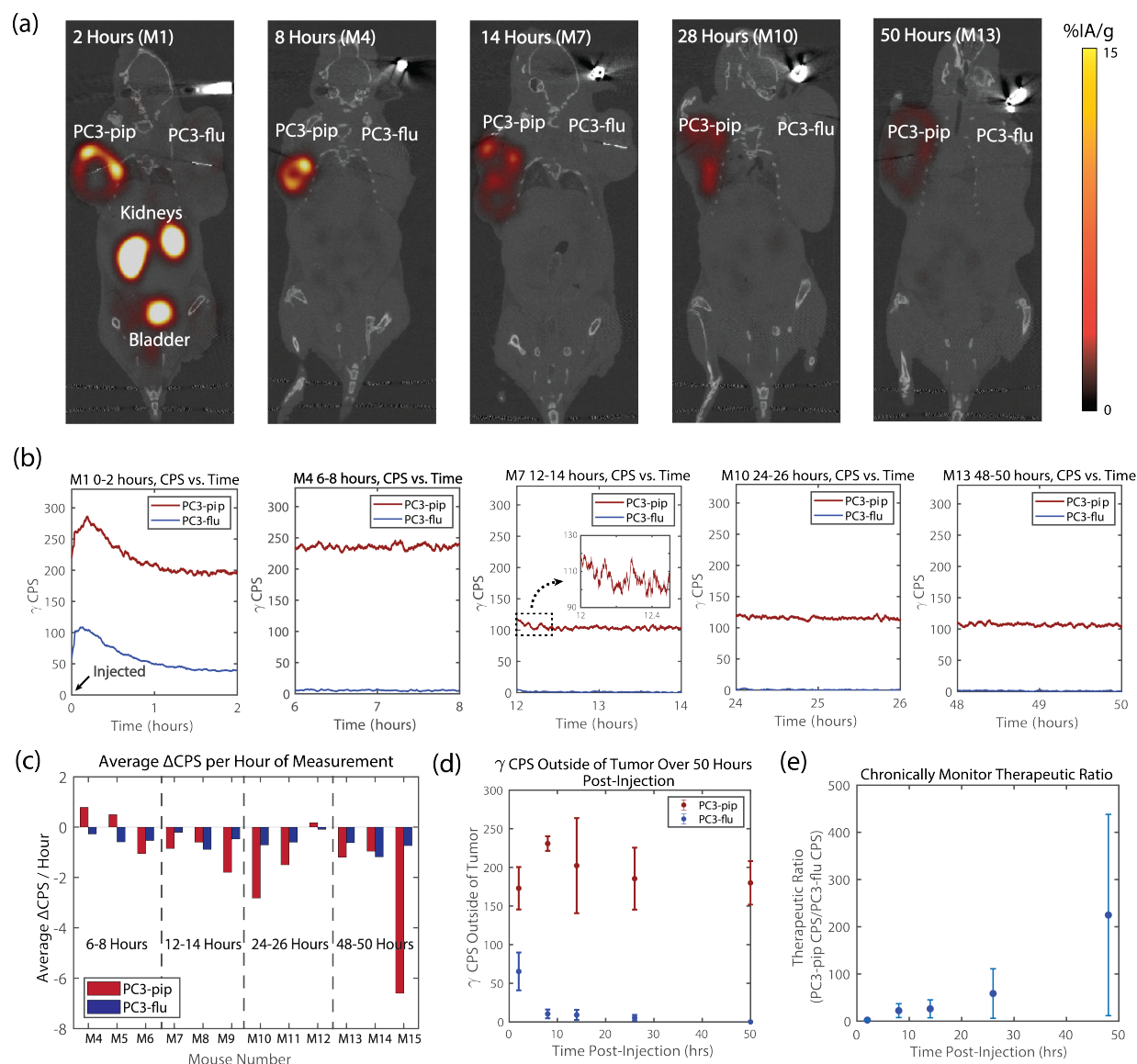


Figure 4.1: Representative SPECT Scans and γ Probe Counts of PC3-pip and PC3-flu Tumors of M1-M15. (a) SPECT scans show progression of ^{177}Lu -PSMA-617 activity accumulation in PC3-pip and PC3-flu tumors at five time points taken at the end of every custom γ probe recording. (b) Real-time γ probe recordings over the two hour recording period before the respective SPECT scan was taken. (c) Average slope of transient waveforms per hour from 6-50 hours post injection. (d) Derived chronic biodistribution curve from proposed system over 50 hours post injection. (e) Therapeutic ratio between the PC3-pip tumor counts to the PC3-flu tumor counts over 50 hours post injection.

4.2 Quantifying Radiopharmaceutical Uptake and Excretion Rates

In understanding how fast the radiopharmaceutical is excreted from vital OARs compared to the target lesions, the instantaneous clearance of the RPT can be approximated with this method, represented by the slope of the transient graph in CPS/hour of recording and calculated for mice M4-M15 (Figure 4.1(c)). The slopes of M1-M3's transient waveforms were not calculated since these plots are not monotonically increasing or decreasing. The transient slope for the PC3-pip tumors of M4-M6 (6-8 h.p.i) were close to zero since this time point has been shown to be the average retention peak of ^{177}Lu -PSMA-617 in PC3-pip tumors *in vivo*. M4 and M5's PC3-pip transient CPS slowly increased with an average slope of 0.79 CPS/hour of recording and 0.5 CPS/hour of recording respectively, while M6 passed the biodistribution peak with PC3-pip transient CPS slope of -1.05 CPS/hour. The average PC3-pip transient CPS slopes of M7-M9 (12-14 h.p.i), M10-M12 (24-26 h.p.i), and M13-M15 (48-50 h.p.i) were -1.08 CPS/hour, -1.38 CPS/hour, and -2.92 CPS/hour respectively, becoming increasingly negative at longer time points post-injection. The PC3-flu transient CPS slopes were always negative and of similar magnitude across time points (for M4-M15). It is important to note that since these mice were under anesthesia for long periods of time, the absolute magnitude of the slopes reported in these mice may be underestimated due to slower respiration and heart rates, and hence slower biokinetics.

4.3 Calculating Therapeutic Ratio

To illustrate the utility of this system in determining therapeutic efficacy (e.g., how much more radiopharmaceutical accumulates per mL of tissue compared to OARs), the average CPS of the last 30 minutes of the 2-hour γ probe recording for mice monitored 2 h.p.i. (M1-M3), 8 h.p.i. (M4-M6), 14 h.p.i. (M7-M9), 26 h.p.i. (M10-M12), and 50 h.p.i. (M13-M15) are plotted in Figure 4.1(d). From these CPS averages, the average therapeutic ratio between the PC3-pip tumor and PC3-flu tumor of mice monitored 2 h.p.i. (M1-M3), 8 h.p.i. (M4-M6), 14 h.p.i. (M7-M9), 26 h.p.i. (M10-M12), and 50 h.p.i. (M13-M15) were computed to be 2.3, 22.4, 26.3, 58.7, and 224.9 respectively (Fig. 4.1(e)).

4.4 Comparison of Measured Tumor Binding Kinetics to State-of-Art Pre-clinical Dosimetry

SPECT/CT

The decay-corrected average activity/mL of tissue from SPECT/CT for the PC3-pip and PC3-flu tumors of mice at each time point are plotted in Figure 4.2(a). If the activity from each of these tumors is plotted against the average CPS from the developed system, there is

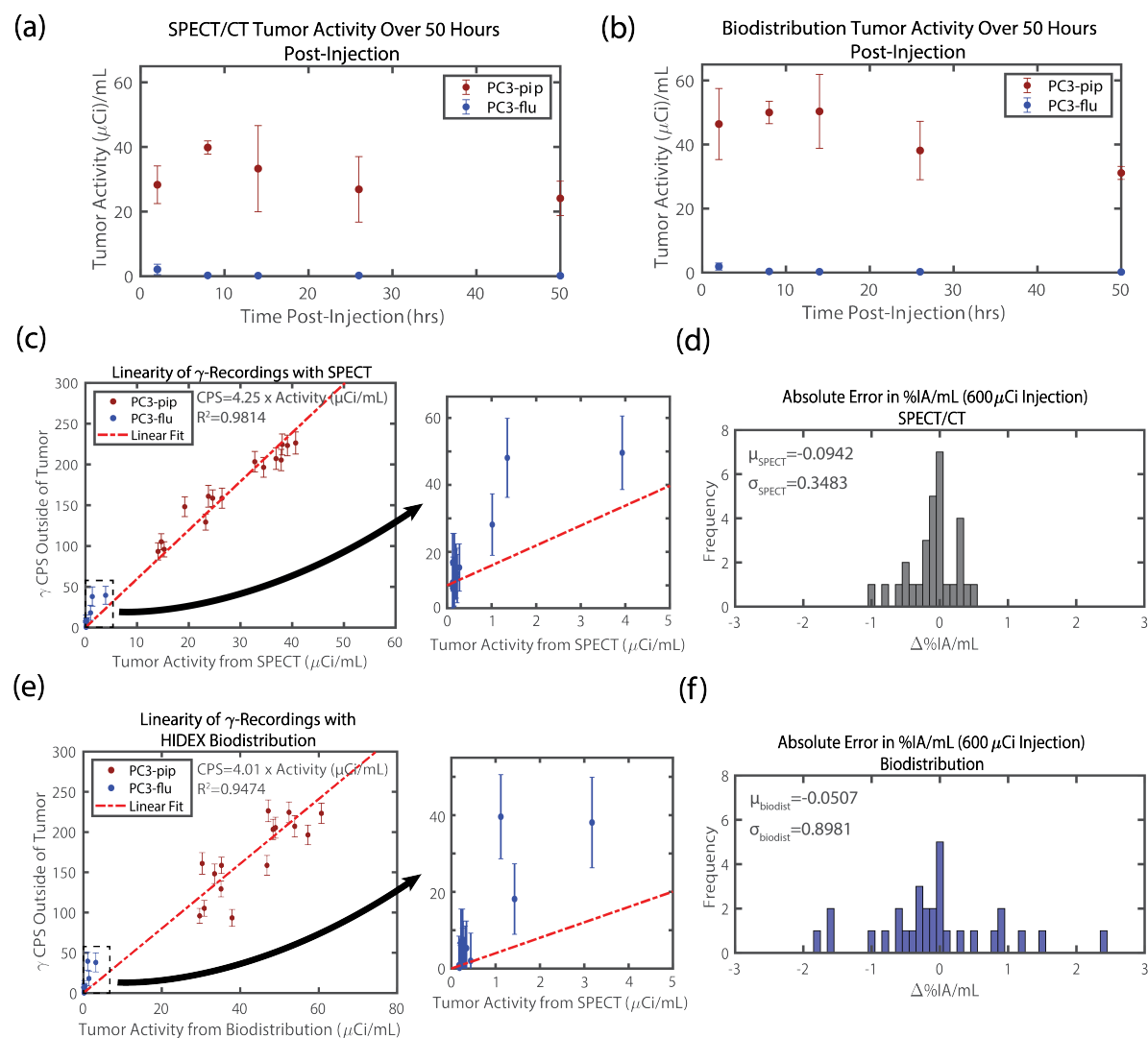


Figure 4.2: Evaluation of Biosensor Accuracy with SPECT/CT and *ex vivo* Dosimetry for M1-M15. Biodistribution curve from (a) SPECT/CT and (b) *ex vivo* dosimetry. (c) Comparison of CPS with the tumor activity normalized to the tumor volume from SPECT. (d) %IA/mL error histogram between the biosensor platform and SPECT/CT. (e) Comparison of CPS with the tumor activity normalized to the tumor volume from *ex vivo* dosimetry. (f) %IA/mL error histogram between the biosensor platform and *ex vivo* dosimetry.

a strong linear relationship between the two. The relationship between tumor activity and average CPS is given by Average CPS = 4.25 (CPS mL/ μ Ci) x Tumor Activity (μ Ci/mL) with an R^2 value of 0.9814 (Figure 4.2(c)). This indicates that the γ probe CPS are accurately tracking the relative changes in tumor activity normalized to tumor volume at each of the time points sufficiently. The error histograms between SPECT and the average biosensor γ CPS for both PC3-pip and PC3-flu tumors are shown in Figure 4.2(d), with a mean error of 0.09 %IA/mL.

***Ex Vivo* Dosimetry**

Similarly, the decay-corrected activity/mL of tissue from *ex vivo* dosimetry for the PC3-pip and PC3-flu tumors of all 15 mice are plotted in Figure 4.2(b). The relationship between tumor activity and average CPS is given by Average CPS = 4.01 CPS mL/ μ Ci x Tumor Activity (μ Ci/mL) with an R^2 value of 0.9474 (Figure 4.2(e)). This further confirms the observation that the γ probe CPS are accurately tracking the relative changes in tumor activity per mL of tissue at each of the time points. The error histograms between *ex vivo* dosimetry and average probe γ CPS for both the PC3-pip and PC3-flu tumors are shown in Figure 4.2(f), with a mean error of 0.05 %IA/mL. The slopes relating the developed system and the tumor activity/mL of tissue have very similar values between SPECT and *ex vivo* dosimetry (4.25, 4.01). The lower R^2 value in the biodistribution study is mainly due to tumor heterogeneity. Since local %IA/mL fluctuates in different parts of the tumor and a section of the tumor volume was measured (to prevent count saturation), extrapolated activity per mL from *ex vivo* dosimetry may vary from the true whole tumor activity per mL.

Chapter 5

Tracking Tumor and Kidney Binding Kinetics Continuously in the Same *In Vivo* Model

5.1 Real-Time Tumor and Kindey Binding Kinetics

After validating the probe-based system against SPECT/CT and *ex vivo* dosimetry, we sought to demonstrate utility for continuous monitoring of biodistribution since this is the intended use case of the system outlined in Figure 1.6. In this experiment, a single mouse (M16) was monitored with one probe on each tumor as before and one probe placed vertically on each kidney for all 5 time points (0-2 h.p.i., 6-8 h.p.i., 12-14 h.p.i., 24-26 h.p.i., and 48-50 h.p.i.) with the probes placed in the same place at each recording time. Each γ CPS recording was scaled to its respective %IA/mL value with a correction factor derived from a single SPECT scan after all the measurements were taken.

The biosensor-measured biodistribution curve (Figure 5.1(a)) and the SPECT/CT biodistribution curve (Figure 5.1(b)) for each tumor and kidney match very well. The mapped %IA/mL from the probe γ CPS measurement is highly linear with the %IA/mL from SPECT, with an $R^2=0.985$ (Figure 5.1(c)), a mean error of 0.20 %IA/mL, and maximum error less than 0.6 %IA/mL (Figure 5.1(d)).

5.2 Approximating Minimum Acquisition Time

To find the minimum amount of measurement time needed for the CPS to converge to that of a 30-minute recording, the amount of measurement time before SPECT was swept from 6 seconds to 30 minutes in 6 second increments. Convergence plots for the average error in %IA/mL, R^2 , and slope of the linear fit are shown in Figure 5.1(e),(f), and (g) as the measurement time is swept from 6 seconds to 5 minutes in 6 second increments before the SPECT/CT. The average %IA/mL error of a shorter measurement converges below the

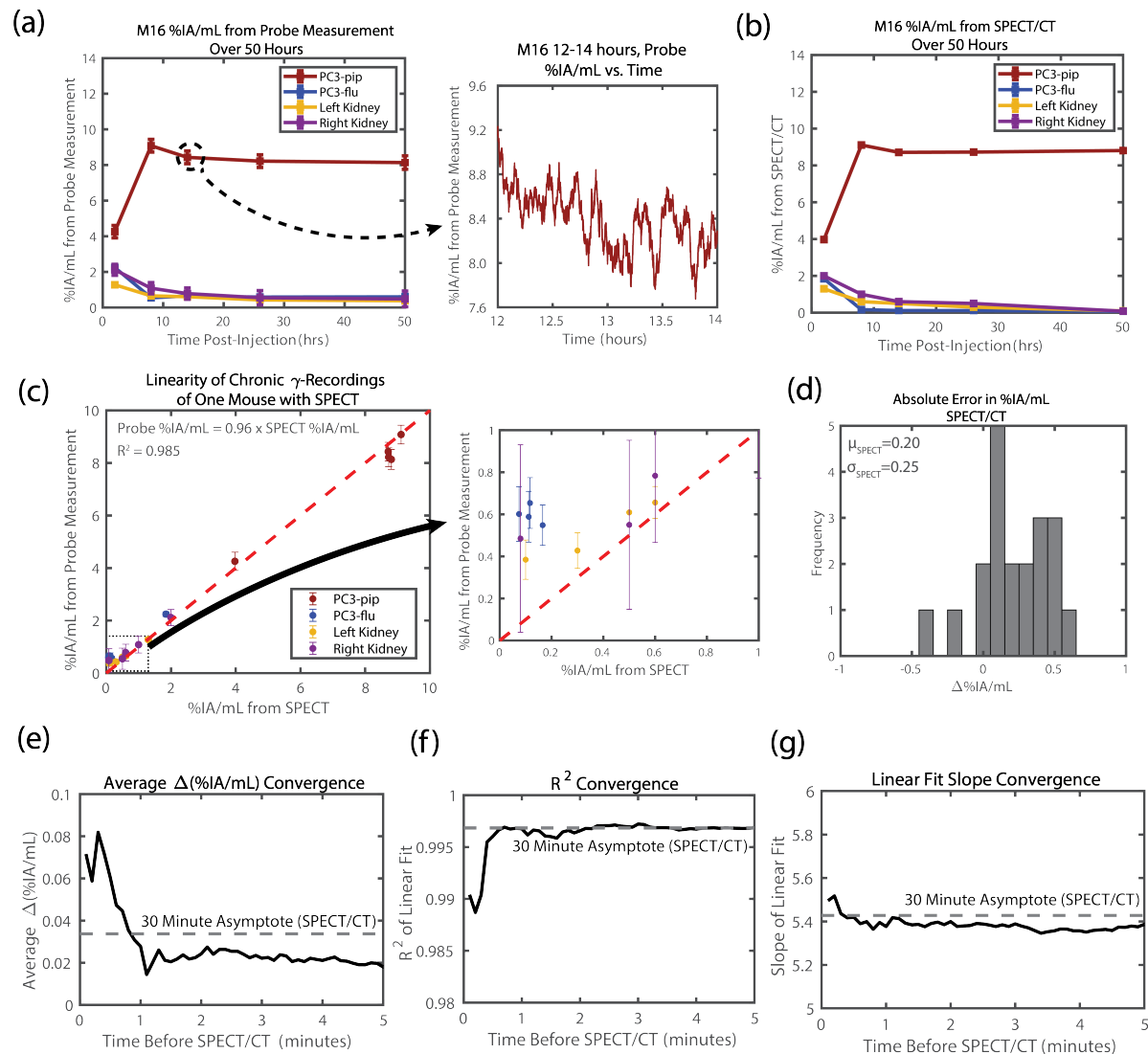


Figure 5.1: Monitoring of a Single Mouse (M16) Over Multiple Time Points. Biodistribution curve from (a) the proposed biosensor platform and (b) SPECT/CT for both tumors and kidneys. (c) Comparison of CPS from the biosensor platform with the activity from SPECT. (d) %IA/mL error histogram between the biosensor platform and SPECT/CT. Convergence in (e) average %IA/mL error, (f) R^2 , (g) and linear fit slope with acquisition time before SPECT/CT.

30-minute asymptote approximately after a 40 second acquisition time, with even shorter acquisitions (down to 6 seconds) still having acceptable average %IA/mL error (Figure 5.1(e)). Similarly, the R^2 converges to the 30 minute asymptote after a 40 second acquisition time (Figure 5.1(f)), with its value acceptable for the minimum recording time tested (6 seconds). The linear best fit line slope fully converges after a couple of seconds (Figure 5.1(g)). Therefore, in the case where the system is used 1 mm away from a tumor or OAR of interest as in the data presented in this study, a minimum recording time of 40 seconds/ $(\gamma$ CPS from ^{177}Lu per mL of tissue) 2 must be used to maintain sufficient signal-to-noise ratio (SNR) to accurately calculate the activity in the tumor or OAR. This means that for a 1 mL tumor with measured flux of 1 γ CPS, a minimum recording time of around 40 seconds is needed, but if a tumor presents with 0.5 γ -CPS/mL, a minimum recording time of 160 seconds is needed. This recording time would have to be increased with approximately the square of the distance away from the tumor (to be conservative).

Chapter 6

Utility of Proposed Biosensor Platform for Pre-clinical Evaluation of Radiopharmaceutical Therapy

6.1 Utility in RPT

This work demonstrates the utility of the developed high temporal resolution, low-cost γ counting biosensor for monitoring real-time biokinetics of RPT in *in vivo* models. This system allows for researchers to understand metrics such as (1) real-time accumulation and clearance rates, (2) accurate dose delivered to tumors and OAR, (3) variance in biodistribution, and (4) real-time therapeutic ratio to pre-clinically evaluate and optimize new RPT candidates.

This study utilized measurements from a ^{177}Lu -based radiopharmaceutical (^{177}Lu -PSMA-617), but this workflow can be seamlessly adapted to other ^{177}Lu -based RPT and lower γ emitting ^{225}Ac -based RPTs (Kruijff et al. 2019, Stuparu et al. 2020, Qin et al. 2020, Kratochwil et al. 2016, Pienta et al. 2008, Carpanese et al. 2020). In the case of ^{225}Ac -based RPT, the γ flux is significantly less due to the lower levels of administered activity (500 nCi) but because of the γ and low-energy X-ray emissions, the detected CPS/ μCi is approximately 13.6x higher (Figure 2.5) when compared to ^{177}Lu . Since the minimum recording time is determined based on the γ flux from the tumor or OAR of interest, the system only requires a 40 second recording time for a tumor with 30 nCi, or 6 %IA/mL.

6.2 System Cost and Scalability

The main problem this platform aims to solve is to provide high temporal information regarding radiopharmaceutical biokinetics in the same model organism and is most powerful when used in conjunction with SPECT/CT or *ex vivo* dosimetry to get high spatial resolution, high temporal resolution, and accurate data over the course of therapy. Although it is

desirable to calibrate each mouse model and the biosensors with one SPECT/CT or *ex vivo* dosimetry measurement at the end of the experiment, the γ counting system can also be used as an affordable alternative (approximately \$6,500 for the platform shown here, compared with \$1,000,000 for small-animal SPECT/CT systems (Ruigrok et al. 2020)) method for lower-cost, more accessible, and faster pre-clinical evaluation of RPT. Although this system measures relative changes in γ CPS, the serial dilution experiment (Figure 2.5(d)) can be used to map the recorded CPS to tumor activity without the use of SPECT/CT or *ex vivo* dosimetry. If this is done with the data collected in Figures 4.2(c), 4.2(e), and 5.1(c), a 1:1.5 mapping between SPECT/CT and tumor activity/mL can be derived. Since the measurements are linear with SPECT/CT, this is a constant factor offset that can be characterized and calibrated out once during system bring-up to find the true tumor activity/mL. Such a significantly cheaper methodology will permit further adoption of pre-clinical evaluation techniques in RPT, especially where conventional small-animal SPECT/CT systems could be cost-prohibitive.

6.3 Limitations

It is important to note that this study utilized customized probe placement to prevent the contribution or cross-talk from γ counts from tumors that are not intended to be measured by a given sensor. The biosensor mitigates this through its lead-shielding which attenuates cross-talk from organs in the same plane as shown in Supplementary Figure 2.6(c)-(d), and if very spatially close organs are being monitored the distance the lead rises above the sensor face can be increased to decrease the field of view of the biosensor and hence decrease cross-talk. In cases where this may not be possible, the other type of cross-talk that needs to be accounted for is cross-talk from multiple radioactive lesions or organs that are in the field of view of the sensor but at different depths. The biosensor inherently mitigates this type of cross-talk when there are multiple high activity organs because of its CPS falloff with distance (Figure 2.6(b)). If needed, any residual cross-talk can be accounted for by correcting the calibration factors (Figure 1.6(c)) that scale the recorded CPS to activity. To correct for the error due to N high activity organs in the field of view of any sensor, N calibration SPECT/CTs can be taken during the course of the treatment to form an N by N system of equations describing the CPS seen at each probe as a linear combination of the activity of each of the N organs in the field of view. This N by N system of equations can be solved to find the corrected calibration factors between CPS and activity without cross-talk. In practice, N is unlikely to exceed 2. Although this is currently a limitation of the system, future work aims to perform real-time dose-reconstruction in many closely spaced tumors and OAR in real-time using a sparse network of these biosensors.

6.4 Comparison to RPT Biosensors in Literature

This work was compared to five relevant works in the area of radiotherapy dosimetry *in vivo*, comparing application, detector type, dynamic range, acquisition time, sensitivity, cross-sectional area, as well as if the sensor provides continuous data, if it has a good transfer function with depth, if it is invasive, if it is capable of multiplexed sensing, if it can detect low flux γ radiation, and if the biosensor had been demonstrated *in vivo*. The innovations made in developing this biosensor are apparent as the sensitivity, acquisition time, dynamic range, and cross-sectional area are all significantly improved compared to the relevant works present in literature (Beyer et al. 2008, Balkin et al. 2014, Kim et al. 2020, Vergnaud et al. 2023, Zhang et al. 2021) as seen in Table 6.1.

	This Work	Tregubov et al. (EJNMI 2023)	Zhang et al. (MDPI Sensors 2021)	Balkin et al. (Cancer Research 2014)	Kim et al. (IEEE Sensors 2020)	Beyer et al. (IEEE Sensors 2008)
Application	RPT Therapy	RPT Therapy	RPT Imaging	RPT Therapy	External Beam Radiotherapy	External Beam Radiotherapy
Detector Type	Optical-Fiber Scintillation Detector	CZT Camera	Scintillation Detector	CCD luminescence detector	Fiber-Optic Calorimetric Dosimeter	MOSFET Threshold Voltage Shift
Dynamic Range of Radioactive Activity	0.5μCi to 500μCi Lu-177	1.5mCi, 3.4mCi, 14mCi of Lu-177 tested	35 μ Ci, 80 μ Ci of Na-22 tested	20 μ Ci to 100 μ Ci of Lu-177	Measures high dose rate (Gy/min range)	Measures high dose (cGy-Gy range)
Acquisition Time	6-40s	1500s	60s/frame	90s	600s	Not Reusable
Sensitivity	0.5μCi Lu-177, 7.8nCi Ac-225	1.5mCi Lu-177 lowest activity tested	35 μ Ci Na-22 lowest activity tested	20 μ Ci Lu-177	Measures high dose rate (5.61 Gy/min)	Measures high dose (0.995 cGy)
Sensor Cross-Sectional Area	4.9 mm²	5038 mm ²	4613 mm ²	729 mm ²	200 mm ²	3.46 mm ²
Continuous data?	Yes	No	No	No	No	No
Depth Sensing?	Yes	Yes	Yes	No	Yes	Yes
Invasive?	No	No	No	No	Yes	Yes
Multiplexed Sensing?	Yes	No	No	No	No	No
γ-Photon Flux	Low	Low	Low	Low	High	High
<i>in vivo</i>?	Yes	No	No	Yes	No	No

Table 6.1: Comparison Table of Related Works in Literature

Chapter 7

Conclusions & Future Work

7.1 Scope of Presented Work

To the best of our knowledge, this is the first work that demonstrates the use of a low-cost, scalable platform of high temporal resolution, high sensitivity γ counting biosensors for monitoring real-time biodistribution of RPT in *in vivo* models. This platform fills key gaps in the current state of the art: (1) high temporal resolution (6-40 seconds) when compared to SPECT/CT (greater than 1800 seconds) enables the monitoring of the real-time fluctuations in tumor activity, (2) several orders of magnitude of cost reduction enables wide spread use, and (3) *in vivo* model-specific data regarding RPT uptake and therapeutic ratio that can be attained in many short acquisition times or over longer periods of time if necessary.

We envision this system and workflow will be utilized to evaluate binding kinetics in real-time, understand and optimize RPT clearance from non-target tissues, and further understand real-time dose modulation in achieving sufficient total integrated dose. This is vital for thorough pre-clinical evaluation of new RPT strategies and their movement to clinical validation.

7.2 Future Work

While trial concepts using dosimetry to guide therapy are being developed, the long lesion retention time and half-life of RPT agents (e.g., ^{177}Lu -PSMA-617) requires a continuous system - monitoring the patient for several half-lives – for accurate and personalized dosimetry. The current state-of-art for patient-specific dosimetry is a hospital-based SPECT scanner which measures the high energy γ photon emissions from radioisotope decay. Currently, patients do not uniformly receive even a single SPECT scan during treatment due to limited accessibility, long scan times, scheduling logistics, and cost, precluding dosimetry for every patient.

For those who do receive a single SPECT, the total dose is estimated by simply fitting the representative biodistribution curve to a single time point measurement (Jackson et al.

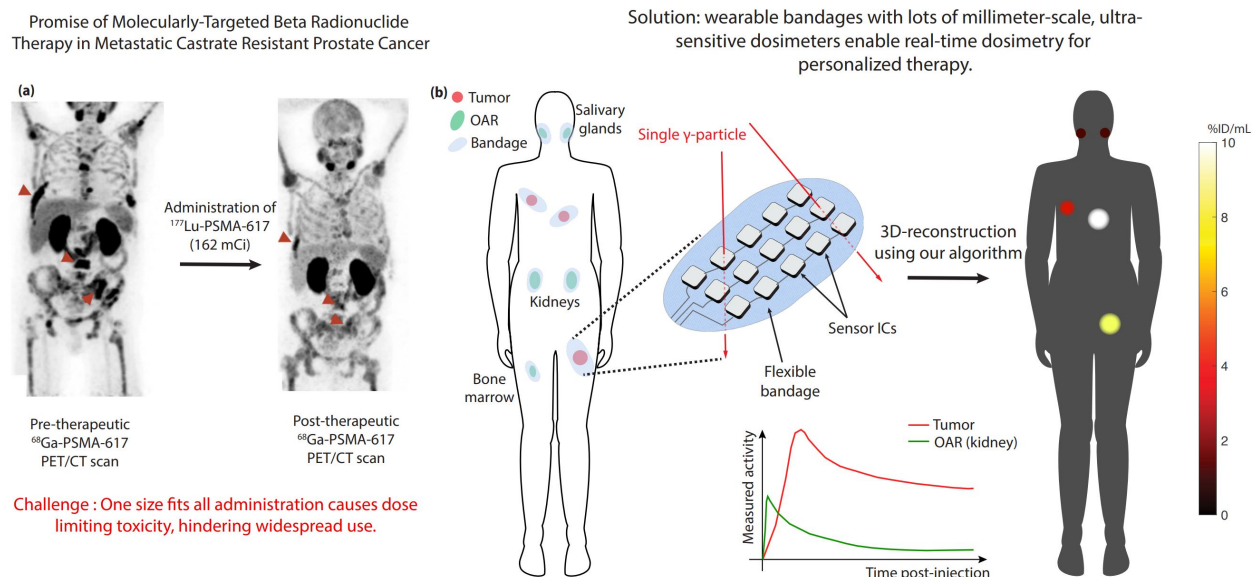


Figure 7.1: Wearable, Integrated Sparse SPECT for Continuous, Real-Time Dosimetry in RPT

2020, Violet et al. 2019). However, this is insufficient as variations in the time to maximum (t_{max}) uptake as well as the effective half-life (T_{eff} the time it takes for the dose to become half) for metastatic lesions can be as high as 50% and 30%, respectively. This uncertainty in dose estimation translates to dose variations of more than 70% over the course of treatment (Peters et al. 2022).

Multi-time point SPECT, for continuous dosimetry, is necessary to observe the full dose distribution and total integrated dosimetry of RPT, but remains a major logistical challenge, and near universally infeasible for patients off of clinical trials (Vallabhajosula et al. 2005). Modern SPECT/CT machines, including the Veriton Multi-CZT Detector and GE StarGuide SPECT/CT systems, demonstrate higher spatial resolution and reduced acquisition time compared to conventional systems. Such systems show promise, but face issues regarding cost, and challenges remain with the complex logistics involved in scanning patients at multiple, optimal, post-injection time points. Moreover, the eventual goal of RPT is to enable wide distribution to the community, where specialized SPECT/CT may not be available.

The long half-lives of these radionuclides and their ligands, the need for accurate dosimetry, and the desire for widespread accessibility of personalized dosimetry, demand the ability to monitor patients outside the hospital setting (i.e., at home), requiring a wearable interface – which, in turn, drives the need for a small form factor, accurate, dosimetry platform. Our proposed solution and future work is to develop a wearable, non-invasive SPECT platform (Figure 7.1) that:

1. Measures dose at all lesions and OARs in a patient, and reconstructs uptake over time.
2. Continuously monitors over days to weeks, driving the need for a wearable network of ultra-thin, lightweight mm-scale sensors, freed from bulky, lead collimators, scintillating crystals, photo-multiplier tubes (PMTs), and power-hungry external equipment.
3. Compatible with at-home measurements, necessary for multi-day measurements. The wearable sensor network would be comfortable enough for everyday use, enabling long acquisition times (for highly sensitive detection) while freeing the patient from hospital visits.
4. Is composed of highly sensitive sensing elements (γ -photon sensitive application specific integrated circuits (ASICs)) to detect γ photons exiting the body, allowing the tracking of biodistribution of a radiopharmaceutical across many half-lives with a small cross-sectional area.
5. Is easily customizable spatial arrangement so that sensor position can be optimized based on a patient's specific lesion and OAR anatomy.

In developing this proposed system, we are working on devising a proof-of-concept algorithm to perform ultra-high temporal resolution dose reconstruction of all tumors and OARs that uptake the therapeutic radiopharmaceutical by utilizing only a sparse network of externally placed γ photon counters. The dose reconstruction method will rely on *a priori* knowledge of tumor and OAR location from a pre-therapy CT scan, reducing the amount of γ photon count information necessary to perform reconstruction and allowing for a sparse network of sensors to be used instead. This proof-of-concept dose reconstruction method will be demonstrated with a sparse network of the optical fiber-based biosensors presented in this Master's thesis, placed around a prostate cancer murine model. Once this has been accomplished, we will scale these optical fiber-based biosensors to mm-scale ASICs to create a sparse wearable network of these on-body sensors, in order to allow for continuous monitoring of dose delivered.

Chapter 8

Bibliography

1. Balkin, E., Kenoyer, A., Orozco, J.J., Hernandez, A., Shadman, M., Fisher, D.R., Green, D.J., Hyalarides, M.D., Press, O.W., Wilbur, D.S., Pagel, J.M., 2014. *Cancer Res.* 74, 5846–5854
2. Bartoli, F., Elsinga, P., Nazario, L.R., Zana, A., Galbiati, A., Millul, J., Migliorini, F., Cazzamalli, S., Neri, D., Slart, R.H.J.A., Erba, P.A., 2022. *Pharmaceuticals* (Basel).
3. Beyer, G.P., Mann, G., Pursley, J., Espenhahn, E., Fraise, C., Godfrey, D., Oldham, M., Carrea, T., Bolick, N., Scarantino, C., 2008. *IEEE Sens J.* 8, 38-50.
4. Bhatt, N.B., Pandya, D.N., Dezarn, W.A., Marini, F.C., Zhao, D., Gmeiner, W.H., Triozzi, P.L., Wadas, T.J., 2018. *Methods Mol Biol.* 1790, 197-208.
5. Carpanese, D., Ferro-Flores, G., Ocampo-Garcia, B., Santos-Cuevas, C., Slavarese, N., Mariangela, F., Fracasso, G., Nardo, L., Bolzati, C., Rosato, A., Melendez-Alafort, L., 2020. *Sci. Rep.* 10, 9313.
6. Choy, C.J., Ling, X.X., Geruntho, J.J., Beyer, S.K., Latoche, J.D., Langton-Webster, B., Anderson, C.J., Berkman, C.E., 2017. *Theranostics.* 7, 1928-1939.
7. de Bono JS, Logothetis CJ, Molina A, Fizazi K, North S, Chu L, et al, 2011. *N Engl J Med.* 364, 1995–2005.
8. Devicor Medical Products, Neoprobe gamma detection system, August 2023, [online] Available: <https://www.mammotome.com/products/neoprobe/>.
9. Dhiantravan, N., Violet, J., Eapen, R., Alghazo, O., Scalzo, M., Jackson, P., et al., 2021. *Eur Urol Focus.*7, 234–237.
10. Duan, H., Iagaru, A., Aparici, C.M., 2022. *Nanotheranostics.* 6, 103-117.
11. Gurp, E.J.B., Haanstra, B.K.C., Murrer, L.H.P., Gils, F.C.J.M., Dekker, A.L.A.J., Mijnheer, B.J., Lambin, P., 2009. *Int. J. Radiat. Oncol. Biol. Phys.* 75, 1266-1272.

12. Halabi, S., Kelly, W.K., Ma, H., Zhou, H., Solomon, N.C., Fizazi, K., et al., 2016. *Journal of Clinical Oncology*. 34, 1652–1659.
13. Herrmann, K., Schwaiger, M., Lewis, J.S., Solomon, S.B., McNeil, B.J., Baumann, M., Gambhir, S.S., Hricak, H., Weissleder, R., 2020. *Lancet Oncol*. 21, e146-e156.
14. Higano, C.S., Schellhammer, P.F., Small, E.J., Burch, P.A., Nemunaitis, J., Yuh, L., et al., 2009. *Cancer*. 115, 3670–3679.
15. Hofman, M.S., Emmett, L., Sandhu, S., Iravani, A., Joshua, A.M., Goh, J.C., et al., 2021. *The Lancet*. 397, 797–804.
16. Hofman, M.S., Emmett, L., Sandhu, S., Iravani, A., Joshua, A.M., Goh, J.C., et al., 2022. *Journal of Clinical Oncology*. 40, 16_suppl-5000.
17. Hotte, S.J., Saad, F., 2010. *Curr Oncol*. 17, S72-S79.
18. Houghton, J.L., Membreno, R., Abdel-Atti, D., Cunanan, K.M., Carlin, S., Scholz, W.W., Zanzonico, P.B., Lewis, J.S., Zeglis, B.M., 2017. *Mol. Chancer Ther*. 16, 124-133.
19. Jackson, P.A., Hofman, M.S., Hicks, R.J., Scalzo, M., Violet, J., 2020. *Journal of Nuclear Medicine*. 61, 1030–1036.
20. Jadvar, H., Chen, X., Cai, W., Mahmood, U., 2018. *Radiology*. 286, 388-400.
21. Kabasakal, L., Toklu, T., Yeyin, N., Demirci, E., Abuqbeitah, M., Ocak, M., Aygün, A., Karayel, E., Pehlivanoglu, H., Alan Selçuk N., 2017. *Mol. Imaging Radionucl. Ther*. 26, 62-68.
22. Keidar, Z., Lugassi, R., Raysberg, E., Frenkel, A., Kennedy, J., Israel, O., 2017, 58, 668.
23. Khosravifarsani, M., Ait-Mohand, S., Paquette, B., Sanche, L., Guerin, B., 2022. *Frontiers in Medicine*. 9.
24. Kim, J., Nam, S.M., Kim, J., Choi, Y., Kim, T.H., Chun, K.J., Chung, H., Lee, W., 2020. *IEEE Sensors Journal*. 20, 5165-5175.
25. Kratochwil, C., Giesel, F.L., Stefanova, M., Benešová, M., Bronzel, M., Afshar-Oromieh, A., Mier, W., Eder, M., Kopka, K., Haberkorn, U., 2016. *J Nucl Med*. 57, 1170-1176.
26. Kratochwil C, Bruchertseifer F, Giesel FL, Apostolidis C, Haberkorn U, Morgenstern A. Dose escalation experience with Ac-225-PSMA-617 in PSMA targeting alpha-radiation therapy of patients with mCRPC. *Eur J Nucl Med Mol Imaging*. 2016;43:S51.

27. Kruijff, R.M.d., Raavé, R., Kip, A., Molkenboer-Kuenen, J., Morgenstern, A., Bruchertseifer, F., Heskamp, S., Denkova, A.G., 2019. *Sci. Rep.* 9, 11671.
28. Ling, X., Latoche, J.D., Choy, C.J., Kurland, B.F., Laymon, C.M., Wu, Y., Salamacha, N., Shen, D., Geruntho, J.J., Rigatti, L.H., Windish, H.P., Langton-Webster, B., Berkman, C.E., Anderson, C.J., 2020. *Mol. Imaging Biol.* 22, 274-284.
29. Malcolm, J., Falzone, N., Lee, B.Q., Vallis, K.A., 2019, *Cancers (Basel)*. 11, 268.
30. McBean, R., O’Kane, B., Parsons, R. Wong, D., 2019. *J. Med. Imaging Radiat. Oncol.* 63, 538-545.
31. Lall, R., Lee, K., Chopra, S., Niknejad, A., Evans, M., Anwar, M., 2022. *Int. J. Radiat. Oncol. Biol. Phys.* 114, e530-e531.
32. Lall, R., Evans, M., Seo, Y., Niknejad, A., Anwar, M., 2023. *Int. J. Radiat. Oncol. Biol. Phys.* 117, S30-S31.
33. Lightpoint Medical, SENSEI Miniature Surgical Gamma Probe, August 2023, [online] Available: <https://senseisurgical.com/>.
34. Moroz, A., Wang, Y.H., Sharib, J.M., Wei, J., Zhao, N., Huang, Y., Chen, Z., Martinko, A.J., Zhuo, J., Lim, S.A., Zhang, L.H., Seo, Y., Carlin, S., Leung, K.K., Collisson, E.A., Kirkwood, K.S., Wells, J.A., Evans, M.J., 2020. *Clin. Cancer Res.* 26, 3608-3615.
35. Nautiyal, A., Jha, A.K., Mithun, S., Rangarajan, V., 2022. *Nucl. Med. Commun.* 43, 369-377.
36. NIST Measured X-Ray Attenuation Coefficient Data, August 2022, [online] Available: <https://physics.nist.gov/PhysRefData/XrayMassCoef/tab2.html>
37. Nussbaum N, George DJ, Abernethy AP, Dolan CM, Oestreicher N, Flanders S, et al., 2016. *Prostate Cancer Prostatic Dis.* 19, 111–21.
38. O’Keeffe, S., McCarthy, D., Woulfe, P., Grattan, M.W., Hounsell, A.R., Sporea, D., Mihai, L., Vata, I., Leen, G., Lewis, E., 2015. *Br. J. Radiol.* 88, 1050.
39. Peters, S.M.B., Hofferber, R., Privé, B.M., de Bakker, M., Gotthardt, M., Janssen, M., et al., 2022. *Eur J Nucl Med Mol Imaging.* 49, 1101–1112.
40. Petrylak DP, Tangen CM, Hussain MHA, Lara PN, Jones JA, Taplin ME, et al., 2004. *N Engl J Med.* 351, 1513–1520.
41. Pienta, K.J., Abate-Shen, C., Agus, D.B., Attar, R. M., Chung, L.W.K., Greenberg, N.M., Hahn, W.C., Isaacs, J.T., Navone, N.M., Peehl, D.M., Simons, J.W., Solit, D.B., Soule, H.R., VanDyke, T.A., Weber, M.J., Wu, L., Vessella, R.L., 2008. *Prostate.* 68, 629-639.

42. Qin, Y., Imobersteg, S., Blanc, A., Frank, S., Schibli, R., B  h  , M.P., Grzmil, M., 2020. *Pharmaceutics*. 12, 1088.
43. Ruigrok, E.A.M., van Vliet, N., Dalm, S.U., de Blois, E., van Gent, D.C., Haeck, J., de Ridder, C., Stuurman, D., Konijnenberg, M.W., van Weerden, W.M., de Jong, M., Nonnekens, J., 2021. *Eur. J. Nucl. Med. Mol. Imaging*. 48, 1339-1350.
44. Sartor, O., de Bono, J., Chi, K.N., Fizazi, K., Herrmann, K., Rahbar, K., Tagawa, S., Nordquist, L., Vaishampayan, N., El-Haddad, G., Park, C.H., Beer, T.M., Armour, A., Perez Contreras, W.J., DeSilvio, M., Kpamegan, E., Messmann, R.A., Morris, M.J., Krause, B.J., 2021. 385, 1091-1103.
45. Satterlee, A.B., Yuan, H., Huang, L., 2015. *Journal of Controlled Release*. 217, 170-182.
46. Scher, H.I., Solo, K., Valant, J., Todd, M.B., Mehra, M., 2015. *PLoS One*. 10, e0139440.
47. Scher, H.I., Fizazi, K., Saad, F., Taplin, M.E., Sternberg, C.N., Miller, K., et al., 2012. *N Engl J Med*. 367, 1187–1197.
48. Stuparu, A.D., Meyer, C.A., Evans-Axelsson, S.L., L  ckerath, K., Wei, L.H., Kim, W., Poddar, S., Mona, C.E., Dahlbom, M., Girgis, M.D., Radu, C.G., Czernin, J., Slavik, R., 2020. *Theranostics*. 10, 2612-2620.
49. Tannock, I.F., de Wit, R., Berry, W.R., Horti, J., Pluzanska, A., Chi, K.N., et al., 2004. *N Engl J Med*. 351, 1502–1512.
50. Tregubov, A.V., Prikhodko, V.V., Alekseyev, A.S., Novikov, S.G., Tertyshnikova, G.V., Zhukov, A.V., 2022. *IEEE Sensors Letters*. 6, 1-4.
51. Vallabhajosula, S., Kuji, I., Hamacher, K.A., Konishi, S., Kostakoglu, L., Kothari, P.A., et al., 2005. *Journal of Nuclear Medicine*. 46, 634–641.
52. Vergnaud, L., Badel, J.N., Giraudet, A.L., Kryza, D., Mognetti, T., Baudier, T., Rida, H., Dieudonn  , A., Sarrut, D., 2023. *EJNM*. 10, 58.
53. Violet, J., Jackson, P., Ferdinandus, J., Sandhu, S., Akhurst, T., Irvani, A., et al., 2019. *Journal of Nuclear Medicine*. 60, 517–23.
54. Woulfe, P., Sullivan, F.J., O’Keeffe, S., 2016. *Cancer Nanotechnol*. 7, 7.
55. Zang, J., Fan, X., Wang, H., Liu, Q., Wang, J., Li, H., Li, F., Jacobson, O., Niu, G., Zhu, Z., Chen, X., 2019. *Eur. J. Nucl. Med. Mol. Imaging*. 46, 148-158.
56. Zhang, Z, Qu, Y., Cao, Y., Shi, X., Guo, H., Zhang, X., Zheng, S., Liu, H., Hu, Z., Tian, J., 2020. *J. Biophotonics*. 13, e201960152.

57. Zhang, X., Xie, Q., Xie, S., Yu, X., Xu, J., Peng, Q., 2021. *Sensors*. 21, 3376.
58. Zhuang, Q., Yaosheng, H., Yu, M., Zhao, W., Weimin, S., Daxin, Z., Ziyin, C., Elfed, L., 2016. *Opt. Express*. 24, 5172-5185.